Towards a High-Efficiency Micro-Thermophotovoltaic Generator

by

Walker Chan

B.S., Massachusetts Institute of Technology (2008)

Submitted to the Department of Electrical Engineering and Computer Science
in partial fulfillment of the requirements for the degree of

Master of Engineering in Electrical Engineering

at the

MASSACHUSETTS INSTITUTE OF TECHNOLOGY

June 2010

Author . . . .
Department of Electrical Engineering and Computer Science
May 7, 2010

Certified by . . . .
John Kassakian
Professor
Thesis Supervisor

Certified by . . . .
Ivan Celanovic
Research Engineer
Thesis Supervisor

Accepted by . . . .
Christopher J. Terman
Chairman, Department Committee on Graduate Theses

Towards a High-Efficiency Micro-Thermophotovoltaic Generator

by

Walker Chan

Submitted to the Department of Electrical Engineering and Computer Science
on May 7, 2010, in partial fulfillment of the
requirements for the degree of
Master of Engineering in Electrical Engineering

Abstract

Hydrocarbon fuels have such a high energy density that even a relatively inefficient converter of chemical energy into electrical can significantly exceed the energy density of state-of-the-art batteries. This work attempts to do exactly this on a millimeter scale by means of thermophotovoltaic (TPV) power conversion approach. We demonstrated the first-of-a-kind propane-oxygen fueled catalytic silicon based MEMS microreactor integrated with low-bandgap GaInAsSb (0.53 eV bandgap) photovoltaic cells to create a fully operational millimeter scale TPV system. The initial fuel to electricity system efficiency was measured at 0.8%. A cell area of 2 cm^2 produced 200 mW of electricity from a chemical input of 28 W. These results match well with developed system models. Additionally, we predict the efficiency can be doubled by improving the view factor, vacuum packaging, and eliminating parasitic radiation from the edges of the reactor. By integrating simple one-dimensional silicon/silicon dioxide photonic crystal on the micro-reactor as spectral shaping device efficiency can reach 5%.

Thesis Supervisor: John Kassakian
Title: Professor

Thesis Supervisor: Ivan Celanovic
Title: Research Engineer

Acknowledgments

First and foremost, I would like to thank Ivan Celanovic. He has been the true driver behind much of this project by providing never ending energy and enthusiasm when faced with one challenge after another. Professors John Kassakian, Marin Soljacic, and John Joannopoulos brought insight and provided a clear vision of the goal even when I was lost in details.

This work would not have been possible without our collaberators. From Lincoln Laboratory, Christine Wang, Robin Huang, Leo Missaggia, and Peter O'Brein made our results possible by providing, packaging, and AR coating the GaInAsSb cells. From Klavs Jesnen's group, Chris Marton was invaluable in reproducing and adapting Brandon Blackwell's microreactor design. Furthermore, he provided me with a crash course in chemical engineering. From LEES Laboraroy, Robert Pilawa designed the maximum power point tracker.

I would like to thank my group mates, especially Peter Bermel and Mohammad Araghchini. Peter did the photonic crystal simulations and optimizations. Mohammad spent some long nights in the fab working on the microreactors. Finally, Nathan Pallo has gone above and beyond his role as a UROP. He built the lab's electrical characterization setup and made many of the electrical measurements used in this work and worked on the maximum power point tracker.

Contents

List of Figures

11

List of Tables

Chapter 1

Introduction

This thesis presents progress towards a 1 watt millimeter-scale propane-fired portable thermophotovoltaic (TPV) power generator about the size of an ordinary butane lighter—a mockup is shown in Fig. 1-1(a). Our motivation is to build a high energy density, small scale, static power source. Indeed, hydrocarbon fuels offer such a high energy density ($\sim$12 kWhr/kg) that a even relatively inefficient generator can significantly exceed the performance of state of the art batteries ($\sim$200 Whr/kg). Traditional heat engines do not scale well, but thermophotovoltaics is promising in small scale applications because they have no moving parts. While still in the research phase, a propane-fueled micro-TPV generator would have obvious applications in extending battery lifetimes for ever increasingly power hungry portable electronics. Consumer, military, medical, and remote sensing devices stand to greatly benefit from this work.

Thermophotovoltaics is a method of converting heat to electricity using infrared light as an intermediary. Combustion heats an emitter to incandescence (see Fig. 1-1(b)) and the resulting radiation is converted by low bandgap, infrared photovoltaic cells known as TPV cells. The obvious difference between solar photovoltaics and thermophotovoltaics is that a TPV system generates its own light. As a result, high efficiency is possible by tailoring the emission spectrum to match the spectral response of the TPV cells. Compared to their solar counterparts, thermophotovoltaics operate at a much higher power densies due to the close proximity of the emitter, and at much lower average photon energy due to the relatively low temperature of the emitter.

(a) Mockup of proposed system   (b) Experimental apparatus in operation
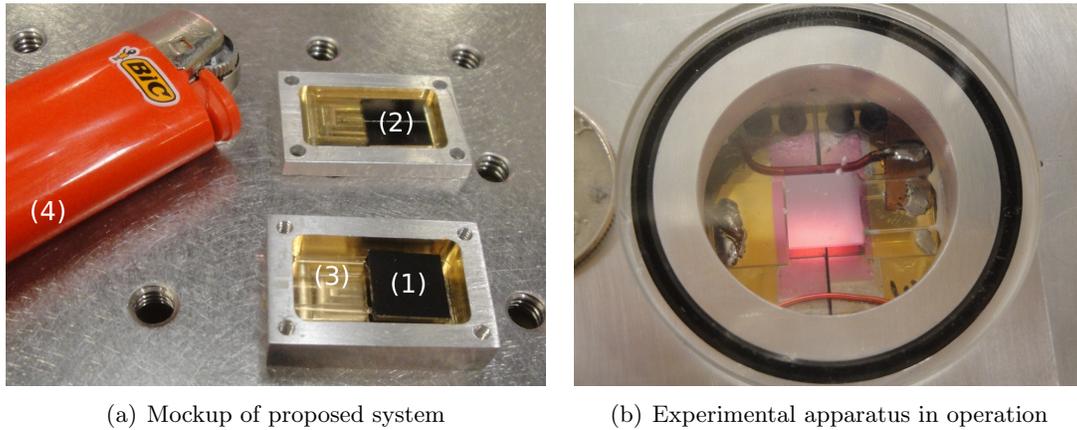
Figure 1-1: A cross section of a mockup of the proposed 1 watt micro-TPV system is shown in (a). The system consists of a MEMS microreactor (1) and low bandgap TPV cells (2). A second set of TPV cells is barely visible under the microreactor. The microreactor is suspended on glass tubes (3). The butane lighter (4) is for scale. The experimental setup used in this work in operation depicting the microreactor (glowing) is shown in (b).

1.1 Portable Power Technologies

We are not the first to attempt to build a high energy density portable power source. This section presents some other technologies being developed. We survey the three major types of generators: electrochemical, thermal, and mechanical. Electrochemical generators includes batteries and fuel cells. Mechanical generators are traditional heat engines such as internal combustion engines and sterling engines where the mechanical energy is used to turn a generator. Thermal generators also use heat energy but have moving parts. The results are summarized in Table 1.1.

Energy densities do not tell the whole story. There are additional considerations such as size, scale, power density, cost, reliability, lifetime, etc. For example, a cordless drill needs high power density and low cost, making batteries a good choice. Soldiers in the field may favor TPV, thermoelectrics, or solid oxide fuel cells for the ability to burn arbitrary fuels. Even if energy density were the sole criteria, Table 1.1 would not be completely fair because some technologies are mature while others are very much in the research phase.

Technology	Energy Density [Wh/kg]	Ref.
Lithium-ion battery	150	[1]
Zinc-air battery	300	[2]
Lithium-air battery	3000	[3]
Direct methanol fuel cell	1100	[4]
Solid oxide fuel cell	7000	[5]
Sterling engine	1500	[6]
Thermoelectrics	750	[7]
Thermophotovoltaics	750	

Table 1.1: Energy densities of portable power technologies.

1.1.1 Electrochemical

Batteries and fuel cells derive electricity from an oxidation-reduction reaction occurring at two electrodes: the negative anode and positive cathode as shown in Fig. 1-2. The electrodes are separated by an electrolyte though which ions but not electrons can pass. Electrons are liberated at the anode where they are forced through the load to the cathode. Ions move through the electrolyte so that there is no charge accumulation. In a fuel cell the reactants are supplied externally and the byproducts are removed, whereas in batteries the reactants are an integral part of the cell.

Lithium-ion batteries

For traditional rechargeable batteries, lithium technology offer the highest energy density. There are many different varieties; we will focus on the lithium-ion battery as an example. In the lithium ion battery, Li^+ ions migrate from one lithium compound at the anode to another one at the cathode and electrons move through the load during discharge. The two lithium compounds have different electrochemical potentials in order to generate the battery's voltage. The anode compound should have a low potential and the cathode should have a high potential to give a large cell voltage. $LiAl$ and Li_xC_6 are good cathodes; $LiMn_2O_4$, $LiNiO_2$, and $LiFePO_4$ are good anodes. For example, the cathode reaction is

$$LiCoO_2 \longrightarrow Li_{1-x}CoO_2 + xLi^+ + xe^- \qquad (1.1)$$

(a) Battery   (b) Fuel Cell
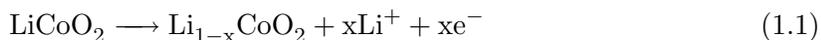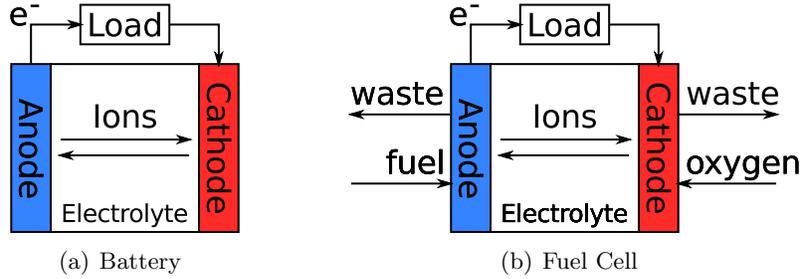
Figure 1-2: Block diagram of a battery and fuel cell.

and the anode reaction is

$$xLi^+ + xe^- + 6\,C \longrightarrow Li_xC_6 \tag{1.2}$$

for a $LiCoO_2$ cathode and a graphite anode. Metallic lithium would make a good cathode except it is highly reactive. During charging, when the Li^+ plates out as lithium metal on the cathode, long dendrites can form, bridge the electrolyte, and short out the cell [1].

Zinc-air and lithium-air batteries

Zinc-air and lithium-air batteries are more accurately described as fuel cells than batteries. High energy density can be achieved because the oxidizer does not need to be stored in the cell. Oxygen from the air is used to oxidize the metal which is internal to the battery. The Li-O_2 cell can potentially have an energy density of 3000 Wh/kg. The anode is metallic lithium, the cathode is porous carbon, and the electrolyte is ceramic [3]. Zinc-air batteries operate on the same principle as lithium-air batteries. The theoretical energy density is 1350 Wh/kg, but in practice is only 200 or 300 Wh/kg. Zinc-air batteries can be recharged by replacing the zinc electrode [2].

Direct methanol fuel cells

Methanol is a desirable fuel because it is readily available, easy to store, and has 50% the energy density of propane. Direct methanol fuel cells (DMFCs) react methanol with oxygen from the air. The methanol is supplied at the anode where it is oxidized

$$CH_3OH + H_2O \longrightarrow CO_2 + 6\,H^+ + 6\,e^- \tag{1.3}$$
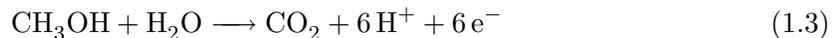
with a Pt-Ru catalyst. Oxygen is supplied at the cathode where a Pt catalyst is often used,

$$\tfrac{3}{2}O_2 + 6\,H^+ \longrightarrow 3\,H_2O \tag{1.4}$$

The H^+ ions move through a proton exchange membrane separating the anode and cathode and electrons move through the load. The water is problematic in DMFCs. The anode needs water to supply the reaction and the membrane needs to stay moist. However, methanol can dissolve in the water and cross the membrane to the cathode where it is oxidized directly. Methanol crossover lowers the cell voltage and wastes fuel [5]. The best power densities reported for microscale DMFC, with comparable size to our TPV system, are in the range from 4 to 30 mW/cm^2 at an energy density of 1100 Wh/kg [4].

Solid oxide fuel cells

Solid oxide fuel cells (SOFCs) operate at high temperatures (around 900°C) and can process naturally occurring fuels directly. The oxidizer is injected at the $La_{1\text{-}x}Sr_xMnO_3$ or $La_{1\text{-}x}Sr_xCoO_3$ cathode where the reaction is

$$\tfrac{1}{2}O_2 + 2\,e^- \longrightarrow O^{2-} \tag{1.5}$$

The O^{2-} ions migrate through the electrolyte and, of course, the electrons move through the external circuit. The electrolyte is yttria-stabilized zirconia and becomes permeable to O^{2-} ions at high temperatures. The other half of the reaction happens at the anode where the fuel is injected. The anode nickel-zirconia cermet where nickel serves as a catalyst. For hydrogen, the reaction is

$$H_2 + O^{2-} \longrightarrow H_2O + 2\,e^- \tag{1.6}$$

and for carbon monoxide it is

$$CO + O^{2-} \longrightarrow C_2O + 2\,e^- \tag{1.7}$$

Complex fuels are reformed to hydrogen and carbon monoxide internally at the anode, then oxidized electrochemically according to the above reactions. A typical hydrogen-oxygen

SOFC would have a voltage of 0.7 volts at a current density of 200 mA/cm^2 at 900°C [5, 8].

1.1.2 Mechanical

Mechanical systems do not scale well because the surface to volume ratio increases thus increasing frictional loses, heat loses, etc. Furthermore, it is difficult to fabricate non-planar structures such as shafts, bearings, valves, and seals at the microscale. Nevertheless, there are several impressive microscale mechanical generators, the most notable of which is the MIT microturbine. Powered by hydrogen, it is designed to generate 17 W of shaft power at 1.2 million rpm in a package the size of a shirt button [9]. On the opposite end of the spectrum, Yale University reported 42.5 W$_e$, 21% efficient JP8-fired stirling engine generator. At 1.7 kg and 400 cm^3, it is hardly microscale but could still be portable [6].

1.1.3 Thermal

Thermoelectric

A thermoelectric element is made of many thermocouples, thermally in parallel and electrically in series, sandwiched between a hot and cold reservoir. The thermocouples are semiconductor junctions rather than metal junctions. Thermoelectrics produce electricity directly from a temperature gradient by the Seebeck effect. When a temperature gradient is applied across a material, a voltage develops at the two ends,

$$V = \alpha \Delta T \tag{1.8}$$

where α is the Seebeck coefficient and ΔT is the temperature difference. A thermoelectric material is characterized by a its figure of merit,

$$Z = \frac{\sigma \alpha^2}{k} \tag{1.9}$$

where σ is the electrical conductivity and k is the thermal conductivity. A higher electrical conductivity leads to higher efficiency because less power is lost to Joule heating. Lower thermal conductivity means less heat can leak from the hot side to the cold side without

generating power. Common thermoelectric materials are SiGe, PbTe, and BiTe. Typical values of Z under 3×10^{-3} [10].

Commercially available thermoelectric generators (TEGs) are available for remote sensing and cathodic protection for pipelines and wells. These units have efficiencies around 6% in power ranges from 10 to 50 W [7]. They are definitely not portable, partly because they are designed to operate for years in harsh environments and partly because they need to dissipate a huge amount of waste heat. Potentially the technology could be adapted. One work on a microfabricated TEG reported an efficiency of 0.02% with a thermal input of 400 mW [11].

1.2 Thermophotovoltaic Technology

The TPV concept was first demonstrated in the 1950s using a Coleman lantern and ordinary silicon solar cells [12]. Poor spectral efficiency was partially responsible for the low overall efficiency, meaning that the overlap between the emission spectrum of the lantern mantel and the spectral response of the solar cells was low. Only photons with energies above the bandgap of the solar cell can be converted into electricity. Thermal emitters at 1000-2000°C are poorly matched to silicon photovoltaics which are better matched to the solar spectrum.

Improved spectral efficiency has only recently been enabled through scientific and technological advancements in two critical areas: low-bandgap semiconductor materials and photonic crystals. Low-bandgap photovoltaic cells convert a much larger portion of the infrared spectrum into electricity, thus enhancing power density [13, 14]. Photonic crystals enable almost perfect spectral shaping, maximizing the efficiency [15]. Furthermore these advances allow a lower temperature (900-1100°C) emitter [16], resulting in reduced thermal stresses, larger spectrum of available materials, and better material stability thus extending the possible design space. With these advances, conversion efficiencies approaching 30% are theoretically achievable.

A thermal to electricity conversion efficiency of 23% at a power density of 0.8 W/cm^2 was demonstrated using InGaAs cells and a cold side filter in a laboratory environment [17]. However, nobody to the best of our knowledge has demonstrated a self-contained TPV

system with an efficiency even close to that figure. Several TPV systems have been demonstrated but they are large and inefficient like their thermoelectric counterparts. The attempts are described below.

- JX Crystals presented work on a 1.5 kW electrical/12.2 kW thermal system based on GaSb cells and a radiant tube burner. The system was large: the cells were operating at 1 W/cm^2 electrical power density. The burner was operating at 1250°C and had an antireflection coated flat tungsten emitter. The overall achievable system efficiency was predicted to be 12% [18].

- NASA built a 25 W propane-fired converter in a 3 inch diameter by 12 inch long cylindrical form factor with an efficiency of 3.0%, although the authors claim efficiencies of 6-7% should be possible [19].

- The National University of Singapore reported a miniature TPV generator using a 150 W hydrogen burner around 1000°C and GaSb cells with a cold side filter. The efficiency was 0.67% [20].

- At MIT, Nielsen designed a microfabricated silicon microreactor that burned propane-air and coupled it with GaSb TPV cells to produce 1 mW of electricity at a system efficiency of 0.08% [21].

Given the state of the art, a measured 1% efficiency is not bad and a 5% predicted efficiency is reasonable. To understand how these systems work, we will look at the individual components: the heat source, spectral control, and TPV cells.

1.2.1   Burners

Macroscale burners

The burners used in the NASA and JX Crystals large-scale TPV systems were cylindrical radiant tube burners [18, 19]. The tube burner was made of two coaxial ceramic tubes of equal lengths. Fuel and air were are allowed to mix partway up the length of the center tube where they burned. The hot exhaust gases flowed out to the end of the inner tube and back in the space between the two tubes. The gases are released from the end of the outer tube.

The length before the combustion served as a simple counterflow coaxial recuperator. The purpose was to transfer heat from the exhaust to the incoming air. The coaxial geometry is not useful for small scale applications because the cells are planar.

Microscale burners

Even MEMS microreactors are sufficiently large compared to the molecular scale on which combustion occurs that same fundamental physics applies, albeit in a different regime. Fluid flow is less turbulent on the microscale, meaning that heat and mass transport occur primarily diffusively. This, combined with the fact that devices are small so the residence time is short, makes complete reactant mixing and combustion difficult. High temperatures are needed to accelerate the reaction to ensure complete combustion. High temperatures are also required to prevent quenching at the reactor walls. Unfortunately, the high surface area to volume ratio makes it difficult to achieve high temperatures. "Swiss-roll burners" solve this problem by surrounding the reaction site by a large circular recuperator. The high surface area to volume ratio also makes catalytic combustion attractive because it is a surface effect. The catalyst lowers the temperature necessary to prevent quenching at the walls. Catalytic combustion is typically slower than gas phase combustion because the reactants must diffuse to the catalyst sites and adsorb, meaning that residence time becomes a bigger factor. Nevertheless, catalytic microreactors are considered easier to implement [22].

The heat source in our TPV system was a microreactor developed by Brandon Blackwell, the SμRE 4 [23]. This microreactor was the most practical in a family of suspended tube microreactors developed by the Jensen Group at MIT [21, 24]. Hereafter referred to simply as the microreactor, the SμRE 4 microreactor was a 10 mm by 10 mm by 1.3 mm silicon slab with a serpentine, platinum catalyst-loaded channel running through it. It was supported by thin glass capillary tubes that also served as fluidic connections to the channel as shown in Fig. 1-1(a). Premixed fuel (propane, butane, and hydrogen were tested) and oxygen were fed into one capillary; carbon dioxide and water vapor were exhausted from the other. There was no recuperation. With a butane flow of 8 sccm (standard cubic centimeters per minute) and 80 sccm of oxygen, the average surface temperature was 850°C. For reference,

Material	Bandgap
Ge	0.66 eV = 1.9 μm (indirect)
GaSb	0.72 eV = 1.7 μm (direct)
GaInAsSb	0.53 eV = 2.3 μm (direct)
InGaAs	0.60 eV = 2.1 μm (direct)

Table 1.2: Bandgaps for TPV materials.

an ordinary lighter burns 15 sccm of butane.

1.2.2   Low Bandgap TPV Cells

Low bandgap PV diodes are a critical component to achieving high efficiency. For a black-body radiator, the electronic bandgap should be around the blackbody peak. Fig. 1-3(a) suggests blackbody peaks for reasonable emitter temperatures fall in the 1.4 to 2.5 μm, thus the bandgap needs to be around 0.5 to 0.8 eV. Table 1.2 gives the bandgaps of four common TPV materials: Ge, GaSb, GaInAsSb, and InGaAs. This work investigates GaSb and GaInAsSb.

Ge (0.66 eV)

Germanium is sometimes presented promising option for TPV cells because of its low bandgap of 0.66 eV and low cost, although the cells are of inferior quality because Ge is an indirect gap semiconductor. Germanium cells are 6-7 times cheaper than GaSb, the next cheapest option. They are made inexpensively by Zn diffusion in an n-type Ge substrate. The quantum efficiency and the open circuit voltage is lower than an equivalent direct bandgap III/V semiconductor, although quantum efficiency can be improved to 90-95% by passivating the front surface with epitaxial GaAs. Additionally, the open circuit voltage and fill factor both drop faster with temperature than III/Vs [25].

GaSb (0.72 eV)

By nature of its direct bandgap, GaSb solves many of the problems with Ge while still being inexpensive. The pn junction can be created by diffusion or epitaxy. For diffusion, Zn is deposited into a Te-doped, n-type GaSb substrate in a closed box then driven in by a

second heating [26]. The GaSb cells characterized in this work were grown at Fraunhofer ISE by metalorganic vapour phase epitaxy (MOVPE). These cells have a 500 nm n-GaSb base, 2500 nm p-GaSb emitter, 50 nm of p-AlGaAsSb window layer, and a two layer MgF_2/Ta_2O_5 antireflective coating on an n-GaSb substrate [14].

InGaAs (0.60 eV)

Epitaxial InGaAs on an InP substrate is a mature technology and generally results in higher quality devices. Because InP has a bandgap of 1.38 eV, it is transparent to the wavelengths of interest and the efficiency can be enhanced by adding a back side reflector. Moreover, the substrate is semi-insulating making it possible to put multiple diodes in series on a single die. These monolithically interconnected modules (MIMs) reduce resistive losses due to lower currents [17].

GaInAsSb (0.53 eV)

The lowest practical bandgaps are possible with GaInAsSb grown epitaxially on a GaSb substrate. The $Ga_{1-x}In_xAs_{1-y}Sb_y$ cells used in this work were grown by MOVPE at Lincoln Laboratory. With $x = 0.15$ and $y = 0.12$, the material has a bandgap of 0.547 eV. The cells have a 1 μm n-GaInAsSb base, 4 μm p-GaInAsSb emitter, a AlGaAsSb window layer, and a GaSb contact layer on a n-GaSb substrate. The cells and growth procedures are nearly identical to those described in [13, 27].

1.2.3 Selective Emitters

Selective emitters are necessary to suppress below-bandgap radiation which wastes heat, cools the emitter, and heats the TPV cells. The natural emissivities of rare earth elements and flat tungsten can be used to do this [18, 28]. This approach of using bulk materials does not leave much room for engineering. On the other hand, a class of metamaterials known as photonic crystals allow tailoring optical properties beyond what is possible with bulk materials.

Photonic crystals are periodic structures with feature sizes on the order of the wavelength of light which allow for novel optical properties not available in bulk materials. A two

(a) Quantum efficiency

(b) Blackbody

(c) Selective emitter
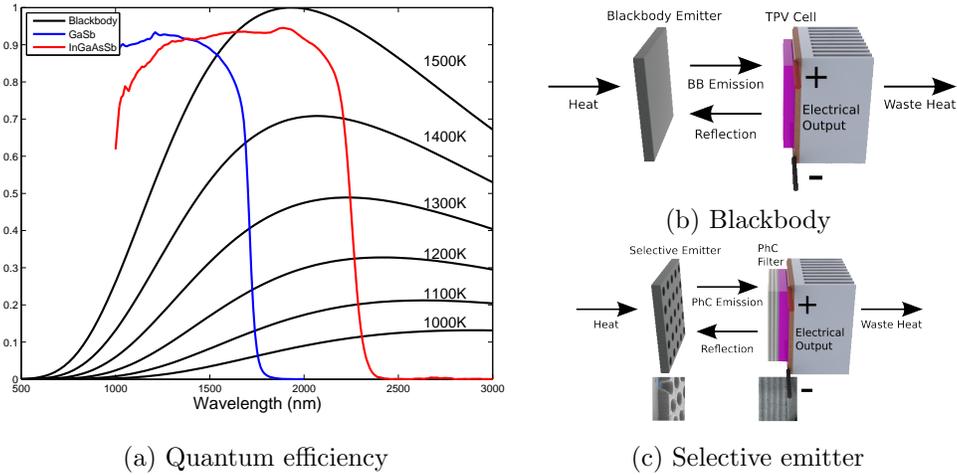
Figure 1-3: Quantum efficiency of GaInAsSb and GaSb cells (a). Cartoon of TPV system with a blackbody emitter (b) and a system with a selective emitter and cold side filter (c).

dimensional photonic crystal for TPV was developed at MIT. The structure was a square lattice of round holes etched in tungsten [15]. An SEM micrograph of the photonic crystal is shown in Fig. 1-3(c). Sandia has fabricated three dimensional tungsten photonic crystals to achieve greater control over the emitted spectrum [29]. Tungsten is chosen for its natural emissivity, refractory properties, and low sublimation rate, but it is difficult to fabricate and integrate. Therefore, we will direct our future efforts to a one dimensional silicon/silicon dioxide stack. Because the microreactor is silicon based, integrating the photonic crystal will be relatively straightforward.

1.3   Thesis Organization

The work done for this thesis involved first developing a generalized multi-physics model of the system. A standard heat balance model was used to describe the microreactor but we were required to develop novel modeling techniques to make the TPV cell model tractable at a system level. The model treated the microreactor, optical cavity (including photonic crystals), and cells at a very high level. For example, it could describe change in efficiency resulting from changing the emitter's emissivity but not the effects of changing the thickness of one of the layers in a photonic crystal.

The second accomplishment was integrating the microreactor and TPV cells to form a

working system. The measured system efficiency was 0.8%—an achievement considering the only other small scale system was 0.67% efficient [20]. Using the system level model and experimental data, we made a detailed investigation into how the other 99% of the energy is distributed. From this investigation, we charted a course to a 5% efficient system by proposing spectral control and mechanical improvements.

The remainder of this thesis is organized in three chapters: modeling, experiment, and future work. Chapter 2 develops a system level model. Chapter 3 describes how the components were characterized and assembled, then how the entire system was tested and the results. Finally, Chapter 4 examines the theoretical and experimental results and makes recommendations on how to move towards the projects goal of a millimeter-scale propane-fueled power source.

1.4 Thesis Contributions

The contributions presented in this work fall into three areas: the TPV cells, the microreactor, and the system. They are described below

- Performed extensive electrical, optical, and thermal characterization of GaInAsSb and GaSb cells. Developed a novel, tractable parameterized model of TPV cells based on the data. The model can predict the performance of a TPV cell under any reasonable operating conditions defined by illumination spectrum and junction temperature.

- Characterized the microreactor and created a heat balance model to calculate its temperature as a function of fuel flow. Coupled this model with the cell model to create a full system level model.

- Reproduced the prior work on the microreactor and made significant improvements to the glass brazing procedure and the packaging.

- Built a TPV system with an efficiency of nearly 1%—an order of magnitude higher than the previous one at MIT. The system is robust enough be demonstrated to laboratory visitors on a regular basis.

These are the four core accomplishments outlined in this thesis. Additionally, the experience gained during the work provided valuable insight into how to move towards the goal of a propane-fueled battery.

Chapter 2

System Modeling

TPV is a very complex system consisting of a microreactor, selective emitter, and TPV cells along with auxiliary components such as fuel pumps, air compressors, cooling systems, and power electronics, as shown in Fig. 2-1(a). Optimizing the complete system is a mixed discrete and continuous[1], multivariate, nonlinear optimization problem that is well beyond the scope of this work. To illustrate this point consider that increasing the size of the heat sink on the cells will increase power output at the expense of weight. Does it make sense to use a large heat sink and operate efficiently or to use a small heat sink and carry additional fuel? Even defining the performance metric is difficult, e.g. what is the trade off between weight and heat signature? In this work, we will analyze existing system components and only discuss these trade offs qualitatively. Specifically, we will discuss the full system shown in Fig. 2-1(a), analyze the system in (b) in detail, and present experimental data for (c).

In order to analyze the system, we partitioned it into three subsystems according to Fig. 2-1: a chemical and thermal, an optical, and an electrical subsystem. The chemical and thermal subsystem model describes the conversion of fuel into heat via the microreactor by analyzing the heat losses. The optical subsystem model describes the thermal radiation transfer from the emitter to the cell. The electrical subsystem model describes the conversion from incident photon flux on the cell into electricity delivered to the load. Together, these three subsystems cover the entire fuel to electricity conversion process.

---

[1]e.g. some discrete variables such as the air pump (either model A or B) and some continuous variables such as microreactor area
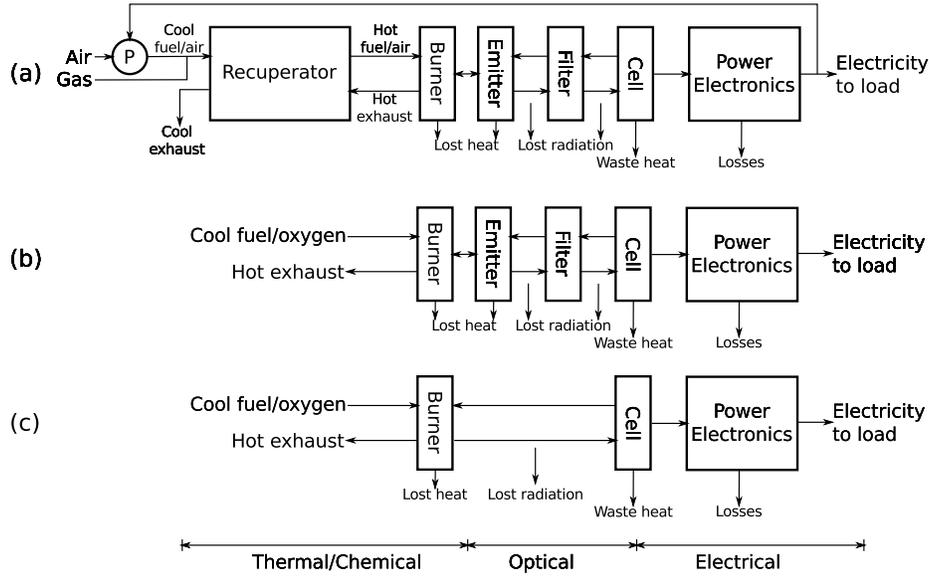
Figure 2-1: A block diagram of a fuel burning TPV system. The full system (a) is air breathing. For detailed analysis, we restrict ourselves to the oxygen-breathing system in (b). The system without spectral control (c) was constructed and tested. In (c) the microreactor itself serves as a greybody emitter.

2.1 Thermal and Chemical Domain Model

This section presents a simple microreactor model based on heat balance. Heat in equals heat out and the temperature dependent heat loss mechanisms allow the temperature to be calculated. The model is zero dimensional because the microreactor is characterized by a single variable, its temperature T_r. The power of this model is that it is largely independent of the specific microreactor design. Thus, we can study system-level interactions without worrying about the inner workings of the microreactor. The heat gain and loss mechanisms are discussed below.

2.1.1 Combustion

The only heat source is the combustion. Assuming complete combustion, the thermal power evolved from burning a stream of flow rate f is

$$Q_{comb} = +(\text{LHV})\, f \tag{2.1}$$

Fuel	LHV [W/sccm]
Hydrogen	0.179
Propane	1.517
Butane	1.974

Table 2.1: Lower heating values of fuels used in this work.

where LHV is the lower heating value of the fuel given in Table 2.1. The lower heating value does not include the energy released when the water vapor in the exhaust in condensed whereas the upper heating value (UHV) does. Under typical fuel flow rates, the combustion generates 20 to 30 W of heat.

2.1.2 Exhaust

Reactants enter the microreactor at ambient temperature, T_a, but the exhaust leaves at the microreactor temperature, T_r. The exhaust loss is equal to the energy required to heat the fuel/oxygen mix to the microreactor temperature:

$$Q_{exh} = \sum_{\text{reactants}} -c_{v,i} f_i (T_r - T_a) \qquad (2.2)$$

where c_v is the specific heat capacity (a temperature dependent heat capacity may be needed) and f is the flow rate. Losses are summed over all reactants i, e.g. propane and oxygen. This formula assumes no recuperation as is the case for us. If a recuperator were added, T_a would be changed to the temperature of the incoming gas after passing through the recuperator. Alternatively, T_r could be changed to the temperature of the exhaust after leaving the recuperator. In our system under typical operating conditions with oxygen and propane, the exhaust losses are 3–5 W.

2.1.3 Radiation

At high temperatures radiation is the dominant heat loss mechanism. Radiation accounts for upwards of 80% of the microreactor's heat loss in our setup. The losses can be divided into two categories: the desirable radiation that enters the optical cavity via the emitter and the undesirable parasitic radiation that comes from the edges of the microreactor or

the brazing compound.

Radiative losses from the emitter must be calculated using the optical cavity model described in Section 2.2 because the emitter can have an arbitrary emissivity and some light can be reflected back to the microreactor from the cold side filter and TPV cell. If the reactor is operated outside the cavity (e.g. it radiates a blackbody spectrum to infinity) or can be well approximated by this situation, then the losses can simply be found with the Stefan-Boltzmann Law.

The parasitic radiation is assumed to be entirely lost, therefore it can be found by the Stefan-Boltzmann Law,

$$Q_{rad} = \sum_{\text{parasitic}} -A_i \epsilon_i \sigma T_r^4 \tag{2.3}$$

where the sum runs over each parasitic source with area A_i and emissivity is ϵ_i. The Stefan-Boltzmann constant is given by σ. The microreactor is 10 mm by 10 mm by 1.3 mm thick. The total surface area is 2.52 cm^2 of which 2 cm^2 radiate towards the cells—80% of the total area. The braze used to attach the capillary tubes to the microreactor has a high emissivity and has radiative losses as well.

2.1.4 Conduction

A small amount of heat is conducted from the microreactor by the capillary tubes according to Fourier's Law,

$$Q_{cond} = -2\frac{kA(T_r - T_a)}{L} \tag{2.4}$$

where k is the thermal conductivity, A is the cross sectional area of the tube, and L is the length. The factor of two accounts for the two capillary tubes. Conduction can be neglected because $A/L \approx 4 \times 10^{-5}$ and the conductivity of Pyrex glass is only 1.1 W/m/K.

2.1.5 Convection

Heat can be transfered from the microreactor by convection when operated in ambient conditions according to Newton's Law of Cooling,

$$Q_{conv} = -hA(T_r - T_a) \tag{2.5}$$
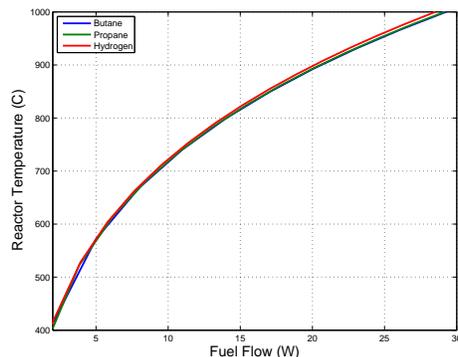
Figure 2-2: Reactor temperature as a function of fuel flow for a 1:1.5 fuel:oxygen stoichiometric ratio for hydrogen, butane, and propane.

where h is the convection coefficient and A is the surface area. Calculating h is beyond the scope of this work. Moreover, convection can simply be eliminated by operating in a vacuum.

2.1.6 Results

The temperature as a function of fuel input is given in Fig. 2-2. The temperature increases more slowly at higher power levels because the radiative heat losses scale as T_r^4. An increase of 100°C around 700°C represents a 50% increase in radiated power. The full breakdown of losses is given at the end of the chapter. Independent of fuel, the reactor temperature is predicted to be 800–1000°C. The specific fuel does not matter because the only difference is the flow rate which effects the exhaust losses. Both the exhaust losses are small and the difference in flow rates are small.

2.1.7 Limitations

The limitations of such a simple model stem from the fact that the microreactor is treated as a point. It was experimentally observed that the microreactor has a nonuniform temperature distribution with a typical range of 100°C. It is unclear how to even choose a single temperature measurement to describe the entire microreactor: should it be an average (linear or T^4 weighting?) of the temperature distribution or should the temperature at a single point be used? We used the temperature at the center of the microreactor be-
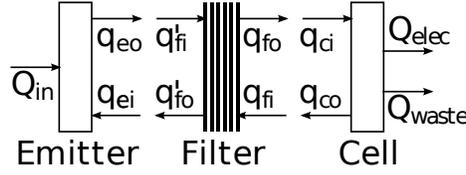
Figure 2-3: The TPV system consists of an emitter, filter and cell. Each component has energy input and output from both sides as shown.

cause it was easiest experimentally. The radiation losses should be strongly affected by the nonuniformity but the model's predictions were surprisingly accurate.

2.2   Optical Domain Model

The optical cavity is the system containing the selective emitter, cold side filter, and TPV cell. The model is responsible for calculating the radiative heat transfer from the emitter to the cell as a function of wavelength. The spectrum incident on the cells is calculated by a detailed balance of the system shown in Fig. 2-3 with a few simplifying assumptions. All emissions, reflections, and even transmissions are assumed to be diffuse. As a result the radiation loss in transit between any two adjacent components is given by the view factor (described below) and there can be no exchange between non-adjacent components. Furthermore, the view factor between the filter and cell is assumed to be unity (e.g. the filter is deposited directly on the cell). The emitter is the only radiating component and has zero transmission. With these assumptions, the spectrum incident on the cell can be found:

$$q_{ci}(\lambda) = \frac{\tau_f F \epsilon_e}{(1 - \rho_c \rho_f)(1 - \rho_e \rho_f F^2) - \rho_c \rho_e \tau_f^2 F^2} e_b(\lambda, T_e), \tag{2.6}$$

where $e_b(\lambda, T_e)$ is the blackbody spectrum of an emitter at temperature T_e, τ is transmittance, ρ is reflectance and ϵ is emittance. The subscripts refer to the components of the system: e for emitter, f for filter and c for cell. For example, ϵ_e is the emissivity of the emitter. The only trick in the derivation is to realize that two optical cavities are formed between the emitter and filter and between the filter and cell. Light can bounce back and forth multiple times giving rise to two infinite geometric series. The full derivation can be found in Ref. [30].
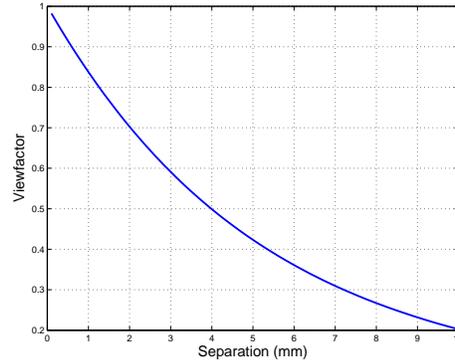
Figure 2-4: View factor between the the 1 cm^2 microreactor and the 1 cm^2 TPV cell array separated by a variable distance. The microreactor and cells are approximated as coaxial disks.

The view factor is simply defined as the fraction of radiated power leaving one component that reaches another. Let F in Eqn. 2.6 be the view factor between the emitter and the filter. Although the actual components are rectangular, the view factor is well approximated by circles of equal area. This approximation is useful because the view factor between two coaxial disks is given analytically by

$$F \quad = \quad \frac{1}{2}\left[X - \sqrt{X^2 - 4\left(\frac{R_2}{R_1}\right)^2}\right] \tag{2.7}$$

$$X \quad = \quad 1 + \left(\frac{1 + R_2}{R_1}\right)^2 \tag{2.8}$$

$$R_i \quad = \quad r_i/d \tag{2.9}$$

where r_i is the radius of disk i (representing either the microburner or cells) and d is the distance between them [31]. The emitter-filter view factor for the system we built is given in Fig. 2-4. It is clear that the microreactor and cells need to be very close, 1–2 mm, to achieve good radiative transfer. Moreover, unless the view factor is close to unity, the cold side filter does not benefit system performance.
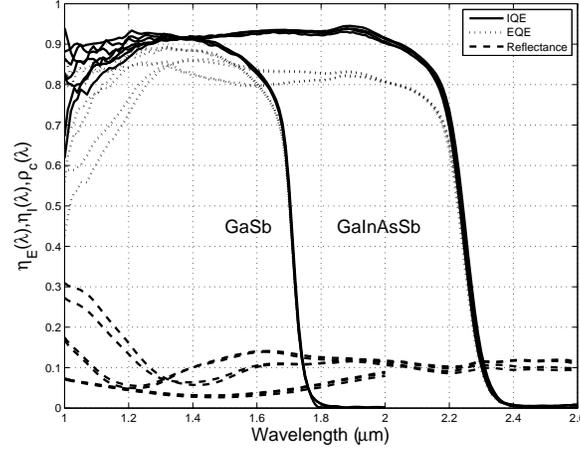
Figure 2-5: Internal and external quantum efficiency and reflectivity measured at room temperature for GaSb and GaInAsSb cells. These data are not corrected for the effects of the bus bar.

2.3   Electrical Domain Model

The cell model converts the optical spectrum incident on the cell into electrical power out and can be divided into two parts: the first converts incident photons into photocurrent using quantum efficiency (QE) and the second converts the photocurrent into a current-voltage (IV) curve using a circuit model. The IV curve serves as a complete electrical description of the DC behavior of the cell.

2.3.1   Quantum Efficiency

Quantum efficiency is the ratio of photocurrent in electron charges to incident photon flux. By this definition the photocurrent is

$$I_{ph} = e \int_0^\infty \frac{\lambda}{hc} q_{ci}(\lambda) \mathrm{IQE}(\lambda) d\lambda, \tag{2.10}$$

where $q_{ci}(\lambda)$ is the radiated power per unit wavelength incident on the cell, hc/λ is the photon energy, IQE is the internal quantum efficiency from Fig. 2-5 and e is the electron charge. There is a distinction between internal quantum efficiency (IQE) and external quantum efficiency (EQE). The former does not include the cell's reflectivity and the later

does,

$$(\text{EQE}) = \rho_c(\text{IQE}). \tag{2.11}$$

We used the IQE in the above formula because q_{ci} already contains the cell's reflectivity.

Measurement

An Optronics Labs OL750 monochromator with a QE accessory and a calibrated PbS detector was used to measure EQE and reflectivity simultaneously. Quantum efficiency was simply measured by illuminating the cell with monochromatic light of known intensity and measuring the short circuit current. Reflection was measured simultaneously by positioning the PbS detector to capture specular reflections from the cell. At the beginning of each measurement session, the monochromatic source was calibrated with the PbS detector.

When using a large spot size (1.5 mm), the front cell contact fingers cause an artificially low EQE and artificially high reflectivity because the cell has a fraction of its area, α, covered by gold fingers:

$$\text{EQE}' = (1 - \alpha)\text{EQE} \tag{2.12}$$

$$\rho_c' = (1 - \alpha)\rho_c + \alpha\rho_{Au} \tag{2.13}$$

The prime indicates a measured quantity and ρ_{Au} is the reflectivity of the gold fingers. The simplest way to handle this is to use the measured QE and the total cell area rather than the true QE and active area when calculating the photocurrent. Unless noted otherwise, this work uses the measured QE and reflectivity in all calculations.

Bandgap Narrowing

Because TPV diodes operate with the majority of photons near the bandgap, a small change in bandgap can result in a substantial change in photocurrent. The bandgap of semiconductor materials depends on temperature approximately as

$$E_g(T) = E_g(0) - \frac{\alpha T^2}{T + \beta}, \tag{2.14}$$
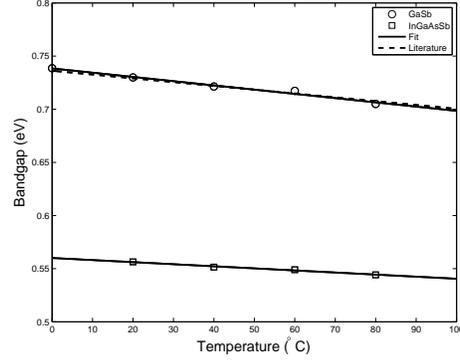
Figure 2-6: Bandgap as a function of temperature.

where α and β are constants [32]. We measured quantum efficiency over temperature and extracted the bandgap from the inflection point in the absorption edge [33]. The temperature dependent bandgaps are shown if Fig. 2-6. Because of the small temperature range, the bandgap narrowing was approximately linear; the results of the linear fit are presented in Table 2.2. The temperature dependence of the GaSb bandgap agrees well with Ref. [34]; whereas the values for our composition of GaInAsSb were not available in literature. To capture the temperature dependent bandgap concisely, the QE is approximated as a step function. For photon energies above the temperature dependent bandgap, the QE is approximated as its average value. Below the bandgap, it is approximated as zero.

Verification

To test the quantum efficiency measurements, the cells were illuminated with blackbody radiation and the short circuit current was measured and reported in Fig. 2-7. The photocurrent can be calculated from Eqn. 2.10 assuming a blackbody source and no cold side filter in Eqn. 2.6. With these modifications, Eqn. 2.10 reduces to

$$I_{ph} = eF \int_0^{\lambda_g(T_j)} \frac{\lambda}{hc} e_b(\lambda, T_e) \, \overline{\text{EQE}} \, d\lambda, \tag{2.15}$$

where $\lambda_g(T_j)$ is the wavelength corresponding to the temperature dependent bandgap taken at the junction temperature, $e_b(\lambda, T_e)$ is the blackbody spectrum, and $\overline{\text{EQE}}$ is the average value of the external quantum efficiency. We calculated the photocurrent due to blackbody
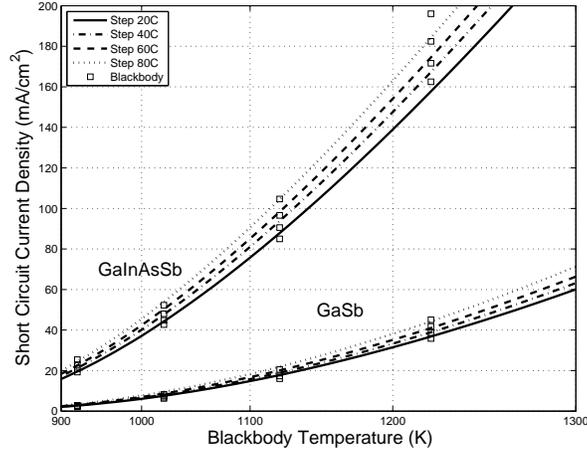
Figure 2-7: Quantum efficiency verification. The cells were illuminated with blackbody radiation and the short circuit current was compared to that calculated with the QE.

radiation in Fig. 2-7. With this model, we captured the increase in current due to increasing blackbody temperature because of σT_e^4 effects and because more of the spectrum is above the bandgap. We also captured the increase in current when the cell temperature increased and the bandgap decreased. Additionally, we see experimental that even a small change in bandgap can significantly change the photocurrent because many photons are near the bandgap.

2.3.2 Circuit Model

The TPV cell can be described by the equivalent circuit in Fig. 2-8(a). The equivalent circuit for an externally illuminated photovoltaic cell consists of a current source representing the generated photocurrent and a diode with parasitic series and shunt resistances. If the photocurrent and all other component values are known then the terminal IV is

$$I = I_{ph} - I_0 \left(\exp\left[\frac{q}{nk_BT_j}(V + IR_s) \right] - 1 \right) - \frac{V + IR_s}{R_{sh}}, \qquad (2.16)$$

where I and V are the terminal current and voltage, q/k_BT_j is the thermal voltage, I_{ph} is the photocurrent, I_0 is the diode dark current, n is the diode ideality factor, and R_s and R_{sh} are the shunt and series resistances [35, 36, 37]. The solutions to Eqn. 2.16 are Lambert-w functions although it is more straightforward to solve the equation numerically.

(a) Terminal IV curve

(b) Diode IV curve
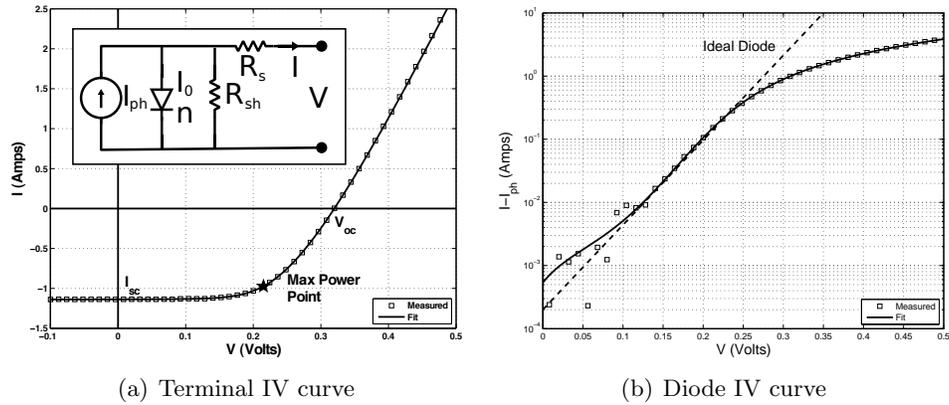
Figure 2-8: Electrical characteristics of a GaInAsSb cell under illumination. The terminal current-voltage relationship is presented on a linear scale in (a). The current through the diode is shown on a semilog scale in (b) in order to emphasize the ideal diode behavior of the cell (dotted line). The circuit inset in (a) is the equivalent circuit used in the model.

Experimental Setup

IV measurements were made in thermal steady state with a Keithley source meter. Photocurrents in excess of $2 \, A/cm^2$ were provided by a 100 W quartz tungsten halogen luminaire energized by a variable voltage power supply. The cells were mounted to a temperature controlled heat sink. Heat sink temperatures between 20°C and 80°C were measured with an embedded thermocouple and maintained by a thermoelectric element. We have made a full matrix of measurements over a temperature range and for all illumination levels. Due to the large volumes of data, we have only reported open circuit voltage (V_{oc}), short circuit current density (J_{sc}), and fill factor (FF) in Fig. 2-9. Open circuit voltage and short circuit current are defined in Fig. 2-8. Fill factor is the ratio of power at the maximum power point to the $V_{oc}I_{sc}$ product.

IV Curve Fitting

The five circuit parameters were found directly from experimental IV curves by fitting to Eq. 2.16. The fitting process used the Nelder-Mead simplex algorithm to minimize a least squares error function [38]. Accurate seeding values were required for the fit to converge. Seeding values were either extrapolated from previously fit data or estimated from limiting cases of the diode equation. For example, neglecting series and shunt resistance,

(a) GaSb fill factor

(b) GaInAsSb fill factor

(c) GaSb open circuit voltage

(d) GaInAsSb open circuit voltage
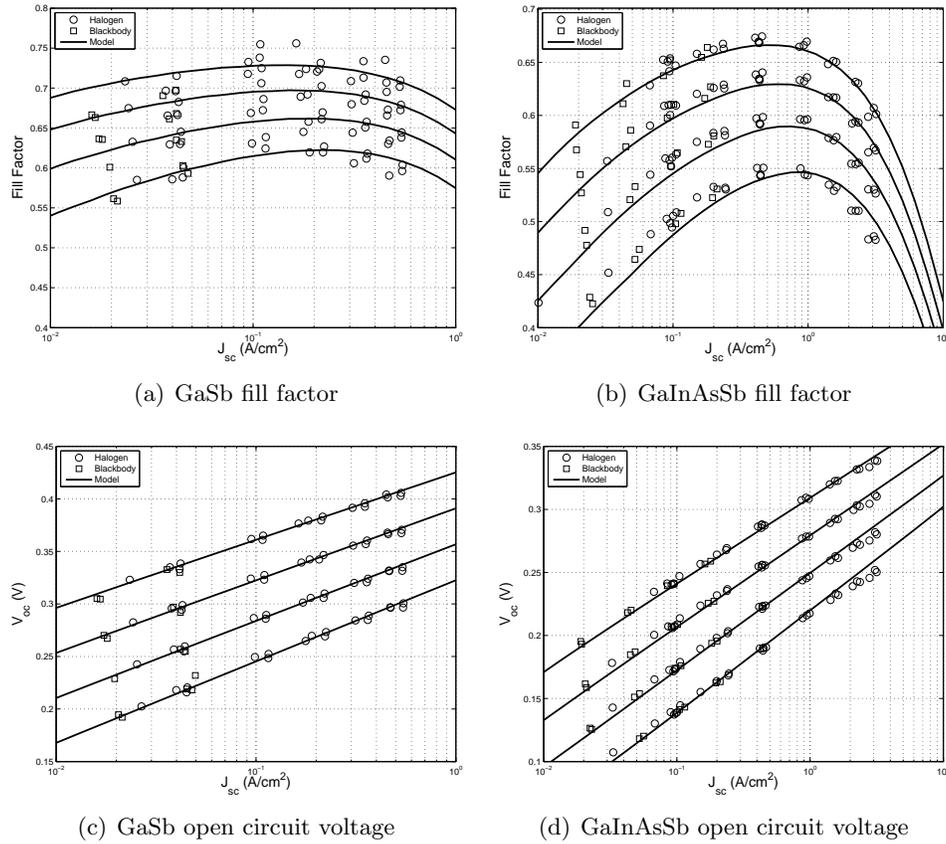
Figure 2-9: Open circuit voltage and fill factor plotted against short circuit current density for GaSb and GaInAsSb cells. Model predictions are overlaid on blackbody and halogen measurements. This was done for cell temperatures of 20, 40, 60 and 80°C, ordered top to bottom in all plots.

the photocurrent is approximately the short circuit current. On the J_{sc}-V_{oc} plot, the slope is related to the ideality and the J_{sc}-intercept is related to the dark current. On individual IV curves, the horizontal asymptote is the shunt resistance and the vertical asymptote is the series resistance. Data was fit on both linear and logarithmic scales. The linear fit in Fig. 2-8(a) emphasizes photocurrent and the parasitic resistances; the logarithmic fit of the diode current $(I - I_{ph})$ in Fig. 2-8(b) emphasizes the diode characteristics. Multiple passes on both axes are required to fine tune all five circuit parameters.

Parameterization

Once a large database of individual equivalent circuits was established (for each combination
of cell temperature and illumination level), we reduced the data further by parameterizing
the equivalent circuits. The goal is to be able to construct an equivalent circuit that is valid
around a specified operating point defined by a photocurrent, I_{ph}, and junction temperature,
T_j. A general relationship between the operating point and the circuit parameters is:

$$
\begin{pmatrix} \ln(I_0) \\ n \\ R_s \\ R_{sh} \end{pmatrix} = \begin{pmatrix} M_{11} & M_{12} & M_{13} \\ M_{21} & M_{22} & M_{23} \\ M_{31} & M_{32} & M_{33} \\ M_{41} & M_{42} & M_{43} \end{pmatrix} \begin{pmatrix} 1 \\ I_{ph} \\ 1/T_j \end{pmatrix},
\tag{2.17}
$$

where the circuit parameters are allowed to have linear dependencies on photocurrent and
inverse junction temperature as well as a constant component.

The parametrization that will give minimum error between predicted and fit circuit
parameters is when all elements of M are fit by least squares. While producing a good fit
within the range of I_{ph} and T_j for which there is experimental data, this technique makes
inaccurate predictions outside the range. Cell heating is at least partially responsible. We
control the heat sink temperature, T_s, but the model depends on the junction temperature,
T_j. The thermal resistance between the junction and heat sink is about 1.0 W/K for a
packaged GaInAsSb cell and comparable for GaSb. At high photocurrents, the temperature
difference can be appreciable, $T_j - T_s \approx 5°C$ for GaInAsSb cells. This was estimated from
the sagging of the J_{sc}-V_{oc} data points in Fig. 2-9(d).

There is no simple method to eliminate the effects of cell heating when all entries of
M are unknown: a change in one of the parameters and an increase in cell temperature
are indistinguishable. The easiest fix is to force $M_{x2} = 0$ whenever M_{x3} is significant.
Photocurrent dependence is ignored whenever a circuit parameter has a strong dependence
on temperature. Thus, $M_{12} = 0$ because we know $I_0 \propto \exp(E_g/kT)$. Furthermore, we
found that we could ignore the entire second and third columns of M except M_{13}. This
simplification neglects certain second order effects. For example, ideality changes with

		GaInAsSb Cells (Lincoln Lab)			GaSb Cells (Fraunhofer)		
Cell No.		01-471-02	01-471-15	01-471-16	01-471-24	1544-41	1544-44	1544-45
$I_0(20°C)$ [μA]		10.8	14.8	11.6	15.1	0.438	0.284	0.376
M_{11}		12.74	13.91	14.09	13.45	17.86	20.16	17.33
M_{13}		-7085	-7333	-7459	-7191	-9522	-10322	-9412
n		1.123	1.171	1.135	1.155	1.106	1.098	1.104
R_s	[mΩ]	29.9	30.5	34.9	34.0	31.0	23.2	38.9
R_{sh}	[Ω]	204	210	372	1182	700	830	500
E_g	[eV]	$0.5548 - (1.952 \times 10^{-4})(T - 300)$				$0.7276 - (3.990 \times 10^{-4})(T - 300)$		
QE		$\eta_I = 90\%, \eta_E = 82\%$				$\eta_I = 89\%, \eta_E = 86\%$		
Area		0.5 cm^2 total, 0.45 cm^2 active				1.55 cm^2 total, 1.40 cm^2 active		

Table 2.2: Model parameters for all cells. Dark current, I_0 depends on temperature as $\ln(I_0) = (M_{11} + M_{13}/T_j)$. All other electrical parameters are assumed to be constant. Quantum efficiency is approximated by a step function with a cutoff wavelength given by the bandgap, E_g, which is a function of temperature.

operating conditions and was observed to slightly vary with the photocurrent [39].

Results

From the equivalent circuits generated by the model, we calculated J_{sc}, V_{oc} and FF. The values of M that were used are listed in Table 2.2. These results are plotted on top of the experimental data in Fig 2-9. Overall, good agreement is achieved. The most notable fact about the fill factor graphs is that it has a maximum. The decrease in FF is due to the cell becoming series resistance limited. The photocurrent translates the dark IV curve down the voltage axis so far that the power producing quadrant only sees the series resistance asymptote. These considerations create an optimum photocurrent density to achieve maximum efficiency.

2.4 Predictions

The three domains were linked to form a complete system model. First, the microreactor heat balance and optical cavity models were solved self consistently. The reactor temperature had to equal the emitter temperature and the net power into the emitter had to satisfy the microreactor heat balance. These two cannot be decoupled because a change in the optical cavity will change the microreactor's heat balance which in turn will change the radiated power. The microreactor temperature is a byproduct of this calculation. Second,
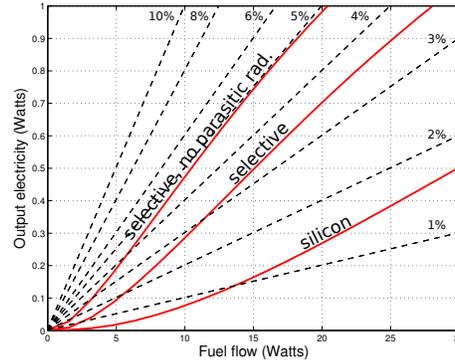
Figure 2-10: Predicted electrical power generated as a function of chemical heat input. The lowest curve is a silicon emitter with a 1mm separation. The middle is a selective emitter. The highest is a selective emitter with reduced parasitic radiation. Black lines are lines of constant efficiency.

(a) Silicon emitter   (b) Selective emitter   (c) Selective emitter, reduced parasitic radiation
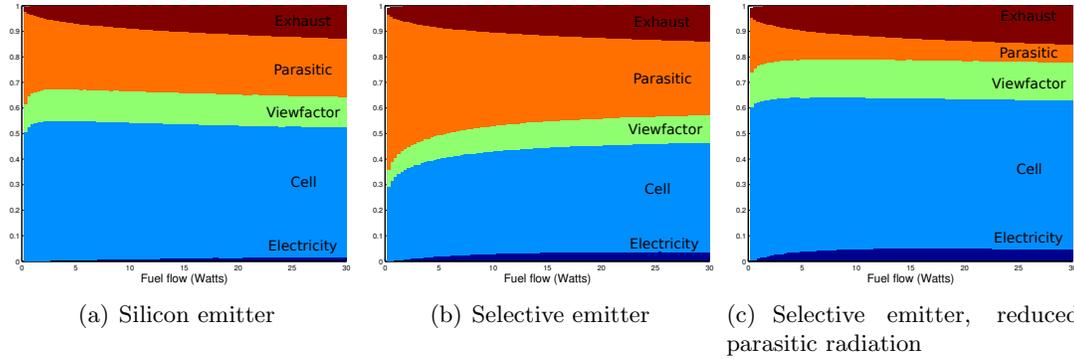
Figure 2-11: Heat loss breakdown. Red is exhaust, orange is parasitic radiation, green is lost radiation due to poor view factor, light blue is unconverted energy incident on the cells, and dark blue is electricity.

the photocurrent was calculated with the quantum efficiency. Finally, the equivalent circuit was calculated from the cell's operating point. The full IV curve was calculated by solving the diode equation. The IV curve yielded the electrical power output, completing the full chemical to electrical model.

Three simulations were performed. The first represents a basic TPV system with a silicon emitter. GaInAsSb cells at 20°C were used. The separation between the microreactor and cells was 1 mm ($F = 0.84$). The predicted power is given by the bottom curve in Fig. 2-10. The calculated efficiency was 1–2%. The heat loss breakdown is given in Fig. 2-11(a). The loss out the exhaust was low because the device is oxygen-breathing. A little less than

half the radiation was lost to parasitic sources or nonunity view factor, but the bulk of the power was lost in the cell, meaning that spectral control would improve efficiency.

The second simulation included a selective emitter. We approximated the selective emitter as a step function. The selective emitter has an emissivity of $\epsilon_e = 0.8$ below the bandgap wavelength and $\epsilon_e = 0.2$ above as well as no transmission at any wavelength, thus $R_e = 1 - \epsilon_e$. These are good approximations considering previous work on photonic crystals as selective emitters [15, 40]. The system efficiency doubled to 3–4%. The peak efficiency with a selective emitter occurred at a lower power level because the system did not need to rely on emitter temperature to shift the spectrum into the convertible range. The parasitic radiation losses increased because the parasitic emissivity was constant but the effective emissivity into the cavity was reduced. It would be helpful to reduce these losses by coating the edges of the reactor with a low emissivity material.

The final simulation assumed that the parasitic radiation from the burner edges was eliminated entirely and the only source of parasitic radiation was the braze. The maximum efficiency jumped to 5%. The maximum efficiency occurred at an even lower power level than the previous simulation. However, the maximum efficiency occurred around the same emitter temperature in both cases. Eliminating the parasitic radiation reduced the amount of power needed to reach this optimum temperature. The heat loss breakdown was similar except the parasitic losses were squeezed by a factor of 3–4.

Chapter 3

System Design and Testing

This chapter describes the process of integrating and testing the TPV system composed of the microreactor and cells. We outline the experimental testing setup, the testing procedure, and the results. Details on the packaging of the cells and microreactor are given in Appendix A and B, respectively. The microreactor fabrication process and masks are found in Ref. [23].

3.1   Experimental Setup

This section describes the experimental setup required to run the microreactors either alone or with the TPV cells to generate power. As shown in Fig. 3-1, the experimental setup consisted of

- A **fuel delivery system** which supplied metered quantities of fuel and oxygen with mass flow controllers.

- A **reactor frame** which held the microreactor above the TPV cells, connected the microreactor to the fuel delivery system, and acted as part of the vacuum chamber.

- A **cell plate** to which the packaged TPV cells were mounted. It served as a heat sinking and as part of the vacuum chamber.

- An **infrared thermometer** was used to measure the microreactor temperature.

(a) CAD Drawing   (b) System in operation
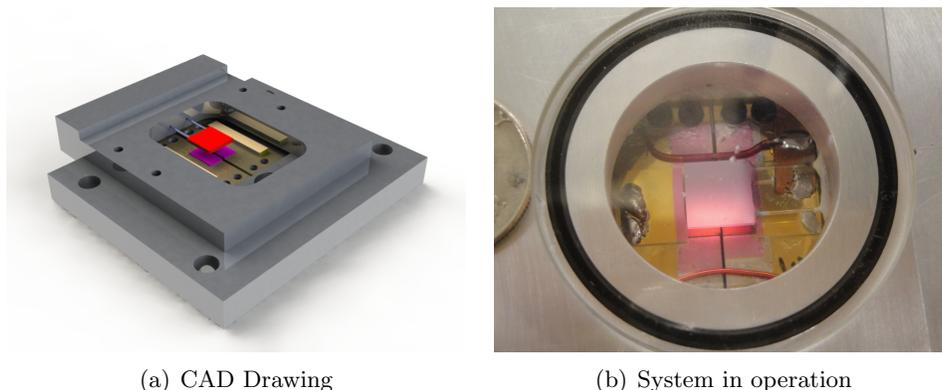
Figure 3-1: Experimental apparatus. A CAD drawing of the system with the top cell plate removed is pictured in (a). In (b), the burner can be seen through the CaF window. The cells are barely visible beneath.

- A custom maximum power point tracker **(MPPT)** and **Keithley** source meter provided the electrical load and measured the power output.

The vacuum chamber was comprised of a reactor frame sandwiched between two cell plates. (The upper cell plates was occasionally substituted for a window to enable infrared thermometry.) The joint between each cell plate and reactor frame was sealed with a Viton o-ring. The chamber was evacuated with a mechanical vacuum pump capable of 10 mTorr. It could rarely be evacuated to 30 mTorr and 100-500 was typical, as measured by a thermocouple vacuum gauge mounted in the vacuum line close to the chamber.

3.1.1   Fuel Delivery

Fuel and oxygen were delivered to the microreactor premixed. Three MKS brand mass flow controllers (MFCs) were used to meter the fuel and oxygen flows. Hydrogen and oxygen had dedicated flow controllers. Butane and propane shared one. The outputs of all the flow controller were tied together at the inlet manifold and were piped to the microreactor. The configuration is shown in Fig. 3-2. The inlet and outlet connection were made to the reactor frame by o-ring seals to the holes shown in Fig. 3-3(a). A pressure gauge was installed in manifold to monitor pressure drop across the microreactor.
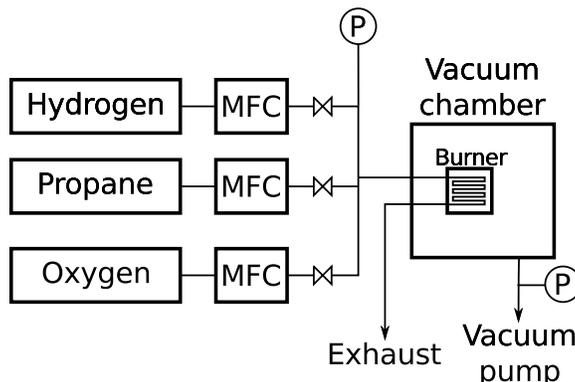
Figure 3-2: Fuel delivery system.

Flashback

To prevent flashback into the MFCs, Swagelok 1/3 psi check valves were installed immediately after each flow controller. Additionally, the entire inlet manifold was plumbed in 1/16 inch stainless steel capillary tubing to quench any flames. We never observed a flame propagating further than the glass capillary tubes, even with hydrogen-oxygen.

Exhaust

Water from combustion can condense at the outlet of the reactor frame. Not only is it a nuisance but it can also clog the glass capillary tube. The exhaust capillary tube from the reactor frame was vented into an exhaust plenum. The plenum was also vented to the atmosphere and connected to the laboratory vacuum through a liquid trap, establishing a flow of 3–4 liters per minute. The airflow vacuumed away any water droplets. The pressure in the plenum was close to atmospheric ensuring that the inlet manifold pressure reading was accurate.

3.1.2 Reactor Frame

The microreactors were mounted in an aluminum frame as shown in Fig. 3-3(a) by the procedure described Appendix B. The frame provided a quick and easy method to replace reactors, protected the microreactor from damage during handling, and allowed for easy connections to the capillary tubes. The thickness of the frame determined the separation

(a) Reactor frame   (b) Cell plate
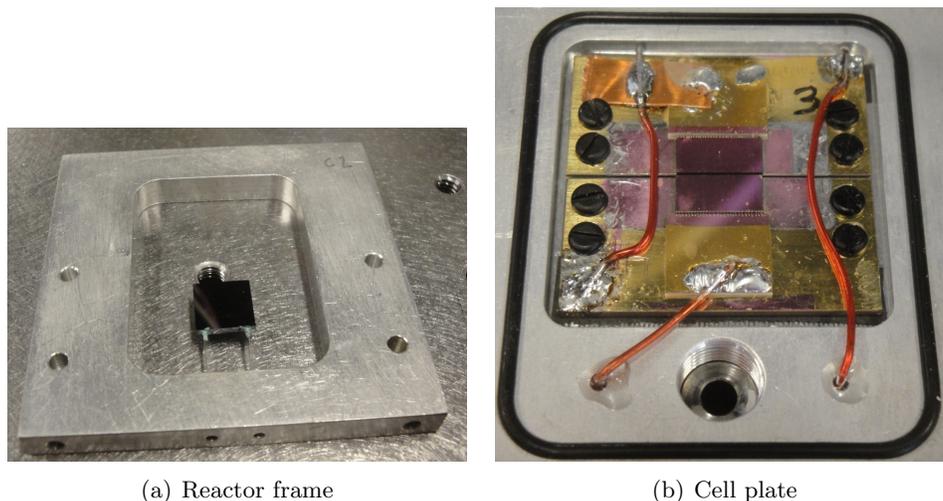
Figure 3-3: The reactor frame with a microreactor and cell plate with cells. Connections to the mircoreactor's capillaries were made through the holes at bottom center. The cell plate has two packaged GaInAsSb cells mounted and wired in series. The vacuum port is visible at the bottom.

between the microreactor and the cells, and thus the view factor. Initially, a 0.500 inch thick frame was employed because of the lack of control over the tubes during the brazing procedure but, with advances described in Appendix B, we migrated to a 0.250 inch frame.

3.1.3   Cell Plate

Two cells are mounted to an aluminum cell plate as shown in Fig. 3-3(b). One cell plate was positioned above the microreactor and one below, for a total of four cells. All were wired in series. A piece of electrically insulating but thermally conducting silicone material furnished by the Bergquist Company provided electrical isolation between the cells and cell plate. No heat sinking is provided aside from the high thermal mass of the cell plate. The plates are of sufficient thermal mass that applying 10–15 W for 30 minutes resulted in a 20–40°C rise. Nevertheless, the cell plate design does not preclude the addition of a chilled water circuit to cool the exterior.
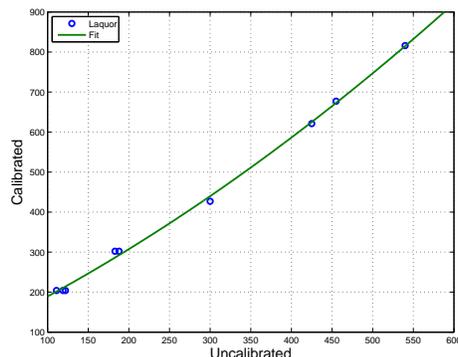
Figure 3-4: IR thermometer calibration curve.

3.1.4 Temperature Measurement

An Optris G5L infrared thermometer sensitive to 5μm thermal radiation was employed to make non-contact measurements of the microreactor's temperature. Blackwell reported that even very fine gauge thermocouples alter the temperature of the microreactor by adding a significant heat loss mechanism [23]. Furthermore, infrared thermometry was desirable for vacuum applications because it necessitates an infrared transparent CaF window rather than an electrical feed-through. In the case that the top two cells replaced by the window, the reported power was doubled to correct for the missing cells. Unless specified otherwise, the measured temperatures are always in the center of the microreactor. This single point measurement proved to produce accurate results despite the nonuniformity seen if Fig. 3-1(b).

The Optris required calibration on pretense of the temperature dependent emissivity of silicon. The calibration was performed by placing a dab of OmegaLaq temperature indicating lacquer on a piece of silicon and applying heat. The OmegaLaq melted at a calibrated temperature and the Optris reading was recorded when it melted. The calibration curve is shown in Fig. 3-4. A sufficient range of lacquer formulations was available to calibrate nearly the entire temperature range.

3.1.5 Maximum Power Point Tracker and Electrical Measurements

Robert Pilawa and Nathan Pallo designed a boost converter with maximum power point tracker (MPPT) controller for this project. The circuit serves two functions: first, it pro-

| (a) Hydrogen | (b) Butane | (c) Propane |
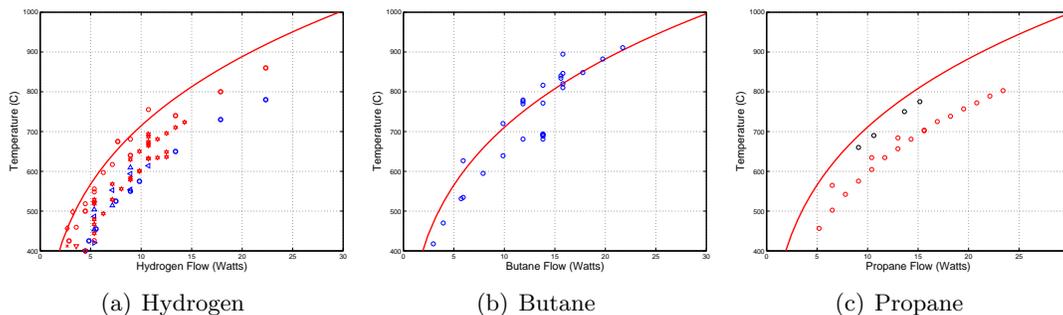
Figure 3-5: Microreactor temperature as a function of fuel flow for hydrogen, butane, and propane. The solid lines are from the heat balance model and the points are experimental.

vides real-time impedance matching between the TPV cell array and the electric load. Second, it boosts the 1 volt output of the array to 3.6 volts–the voltage of a lithium battery. The converter has 90% conversion efficiency and 99% tracking efficiency. Tracking efficiency measures how closely the MPPT tracks the true maximum power point of the cells. Conversion efficiency is the ratio of output to input electrical power [41].

When operating with the MPPT in place, the output power was simply the output voltage times the output current. We used a Keithley model 2440 source meter as a constant voltage electronic load. When operating without the MPPT, the Keithley was used to sweep an IV curve of the entire array in the same fashion individual cells were characterized. The maximum power point was calculated from the IV curve and that number was reported. The MPPT has the obvious advantage of providing a real-time readout of power generated.

3.2   Microreactor Testing

When operating with hydrogen, the microreactor could be lit by merely flowing the reactants at room temperature. For propane and butane, the microreactor had to be preheated to about 300°C by co-feeding a small amount of hydrogen along with the propane or butane until the reaction became self sustaining. Once the microreactor was lit, the fuel and oxygen flow were increased gradually and data was recorded. Oftentimes, the microreactor was run until failure. Data for all fuels is presented in Fig. 3-5. The range of temperatures for a given fuel flow is large because of variation in vacuum level. Data points at higher

temperatures correspond to higher vacuum and the ones at lower temperature were taken closer to ambient conditions.

3.2.1 Hydrogen Combustion

Homogeneous combustion proved to be a problem at high temperatures and flow rates. The mixture would flash back into the glass capillary causing them to fail catastrophically. Flash back could be mitigated by moving to higher and higher oxygen flow rates. High temperatures could only be achieved with six times the stoichiometric oxygen flow, leading to inefficient operation and excessively high flow rates.

3.2.2 Butane Combustion

Butane proved to be much more stable than hydrogen. Homogeneous combustion was never observed with a 1.5 times stoichiometric ratio (a lean mixture) due to butane's lower flammability. One of the difficulties encountered during system testing was that the microreactor experiences occasional temperature fluctuations due to condensed butane entering the fuel supply. Butane is delivered to the microreactor as a gas but occasional droplets, representing additional fuel, can enter the inlet stream. When a droplet enters the microreactor, there is a sudden increase in temperature as it burns. Ref. [41] presents a graph of the MPPT tracking the changing microreactor temperature during one of these events. The temperature increase is often benign but can sometimes cause the braze to crack due to thermal shock.

3.2.3 Propane Combustion

Propane was the most stable fuel tested. We never observed homogeneous combustion or condensation. Like butane, propane was also burned at a 1.5 times stoichiometric ratio, though the mixture did not flash back even with a stoichiometric mixture. Propane has a higher vapor pressure ($\sim$10 atm) compared to butane ($\sim$1 atm), eliminating the condensation problem.

(a) Power   (b) Heat loss
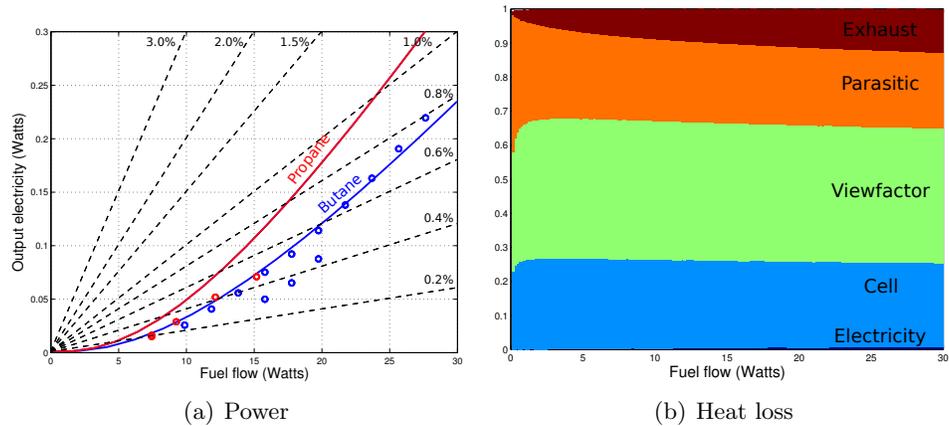
Figure 3-6: Experimental power as a function of fuel flow. Experimental data for propane and butane is shown as points and model predictions are solid lines. Propane is higher because we increased the view factor before making the switch, not because of an intrinsic property of the fuel. The black lines are lines of constant efficiency. The heat loss breakdown is plotted for the propane case.

3.3   System Testing

The experimental results are shown in Fig. 3-6(a). The peak measured efficiency is 0.8%. The discrepancy between the measured and predicted power is probably due to the difference in temperature discussed in the previous section. In fact, the propane curve "falls" away from the model as the power increases. The epoxy began to burn and the level of vacuum decreased, decreasing the microreactor temperature. The three points on the butane curve that lie beneath the rest were taken in ambient; the others were taken in vacuum.

The difference between the propane and butane data is due to changing view factors not fuels. The propane data was taken with a microreactor to cell distance of about 3 mm and the butane data was taken at about 5 mm. These figures are not exact because the microreactor position varies from run to run. It depends on how the tubes were brazed and how it was epoxied into the frame. Moreover, the rubber o-rings used to seal the vacuum chamber compress when under vacuum, bringing the microreactor closer to the cells.

The heat loss breakdown in Fig. 3-6(b) shows the best areas to work on. Improving the view factor and reducing the parasitic radiation losses are relatively easy ways to improve efficiency. Although not visible from the figure, vacuum packaging will reduce convection

losses that are not included in the model, allowing the experimental power generation to approach the model predictions. Finally, spectral efficiency can be improved with a photonic crystal emitter.

Chapter 4

Conclusion and Future Work

The primary areas, alluded to in the previous section, where we can work to improve efficiency are listed below.

1. Improving the **view factor** by reducing the separation between the microreactor and cells.

2. Reducing **parasitic radiation** by coating the sides of the microreactor with a low emissivity material.

3. **Vacuum packaging** the reactor and cells to eliminate convection.

4. Improved **cell packaging** to keep the cells cooler and simplify system integration.

5. Improving spectral efficiency by depositing a **photonic crystal** selective emitter directly on the microreactor.

The first four improvements are relatively simple but taken together should double the efficiency. These all relate to improving the packaging so that the current system can approach the maximum possible efficiency with our geometry, emitter material, etc as determined by the laws of physics. The fifth item is somewhat challenging but will give another twofold improvement by suppressing radiation loss from the microburner and reducing thermal load on the cells. The first two sections of this chapter are devoted to packaging and the photonic crystal. In the last section we look at the challenges associated with realizing the our goal of a truly portable high energy density power source.

4.1   Packaging

There is an easy factor of two in system performance from improved packaging. Reducing the distance between the microreactor and cells will improve the view factor. Coating the microreactor edges will reduce parasitic radiation. Sealing the cavity so that high vacuum can be achieved will increase microreactor temperature. Furthermore, high vacuum is necessary to prevent metallic photonic crystals from oxidizing. Finally, improved cell mounting will lower the cell temperature, slightly increasing efficiency.

4.1.1   Improved View Factor

The data in this work were taken with 0.500 or 0.250 inch thick reactor frame. The microreactor-cell separations were approximately 5 and 3 mm,[1] corresponding to view factors of 0.4 and 0.6, respectively. Such thick plates were necessary before the new brazing jig was developed. The switch to 0.125 inch plates is straightforward and could increase the view factor to 0.7-0.8.

4.1.2   Elimination of Parasitic Radiation

A large amount of heat is radiated to the sides. This could be reduced substantially by coating the sides of the microreactor in a low emissivity material. Some high reflectivity, high temperature paints from Aremco may be suitable although their adhesion to silicon and optical properties will need to be characterized.

4.1.3   Vacuum Packaging

There is no fundamental reason that the microreactor cannot be operated in high vacuum because it is entirely silicon and glass. The epoxy used to seal the tubes to the reactor frame was the weak link. It burned after 20-40 minutes of runtime at high power levels. The tubes are likely reaching ∼300°C based on a study of the thermal degradation of the epoxy. Polymers do not work well in vacuum because of out gassing. Even if the epoxy

---

[1]The amount the cells were recessed into the cell plates also changed.

does not burn, it will out gas when heated. The epoxy needs to be replaced by a more temperature resistant and vacuum friendly material such as metal, glass, or ceramic.

One solution is to return to a silicon frame like was originally used then abandoned [23]. The same glass brazing technique can be used. Glass brazing is a proved technique for high vacuum and is used to bond the front panel to the tube in CRT monitors. Another solution is to use a ceramic adhesive such as those produced by Aremco. However, they are typically porous and need a secondary coating to make the seal vacuum tight. Yet another solution is to metallize the glass tubes (by sputtering, evaporation, or chemical methods) and use a metal solder [42, 43].

4.1.4   Improved Cell Packaging

The cells are currently mounted on copper submounts that serve as the negative contact. This arrangement is suitable for testing individual cells but using multiple cells in parallel is problematic because the submounts must be isolated. The silicone layer providing electrical isolation has poor thermal conductivity and the copper submounts are too big to use in an miniature system. TClad copper core PCB from the Bergquist Company offers lower thermal resistance and the ability to pattern arbitrary interconnects between cells.

4.2   Photonic Crystal

A multilayer silicon/silicon dioxide interference filter can potentially double the efficiency by reducing above-bandgap. Peter Bermel optimized the structure given in Table. 4.1 which has radiation spectrum shown in Fig. 4-1. These layers can be deposited by plasma enhanced chemical vapor deposition (PECVD) directly on the microreactors. This can be done using the DCVD tool at MIT's Integrated Circuits Lab (ICL) clean room according to the process in Appendix C. The layers deposited by PECVD are generally low quality and need to be annealed. The film's thickness and index of refraction change during the annealing process, necessitating careful measurements of the film properties before and after annealing.

Layer	Material	Thickness [Å]
1	SiO_2	2749
2	Si	2356
3	SiO_2	5498
4	Si	2344
5	SiO_2	5469
6	Si	2331
7	SiO_2	5439
8	Si	2319
9	SiO_2	5410
Si substrate		

Table 4.1: Structure of proposed photonic crystal (from Peter Bermel).
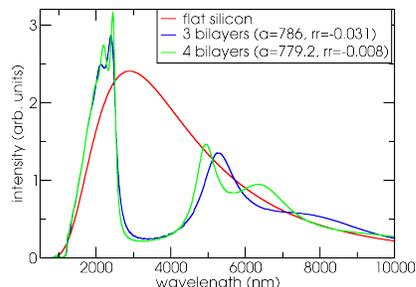
Figure 4-1: Radiation spectrum of proposed photonic crystal (from Peter Bermel).

4.3   Towards a Portable Power Source

The results of these improvements are shown in Fig. 4-2(a). The improved packaging boosts the efficiency to 2% and the photonic crystal boosts it to 5%. The breakdown of heat losses for the system with improved packaging and the photonic crystal is shown in Fig. 4-2(b). To understand what the 5% efficiency number represents, let's put it in concrete terms. To generate one watt of electricity, the system needs to burn 1.5 grams of propane or butane per hour, or 2–3 milliliters of liquid fuel in an hour. Thus, a standard 20 pound propane barbecue tank could provide 1 watt of power for over half a year. It would require 65 pounds of lithium batteries or over 100 pounds of alkaline batteries to deliver the same amount of energy.

This analysis ignores one important factor: the current microreactor is oxygen breathing, not air breathing. By stoichiometry, the 20 pound barbecue tank would require 72 pounds of oxygen to burn, for a total of 92 pounds not including the generator. Lithium batteries become better in every respect and alkaline batteries become equivalent in terms of energy density, not to mention orders of magnitude cheaper and simpler.

This analysis demonstrates that if we hope to build any sort of portable power generator we need to redesign the microreactor to be air breathing. There are two additional considerations for an air-breathing microreactor: recuperation and pressure drop. Because

(a) Power output   (b) Heat loss

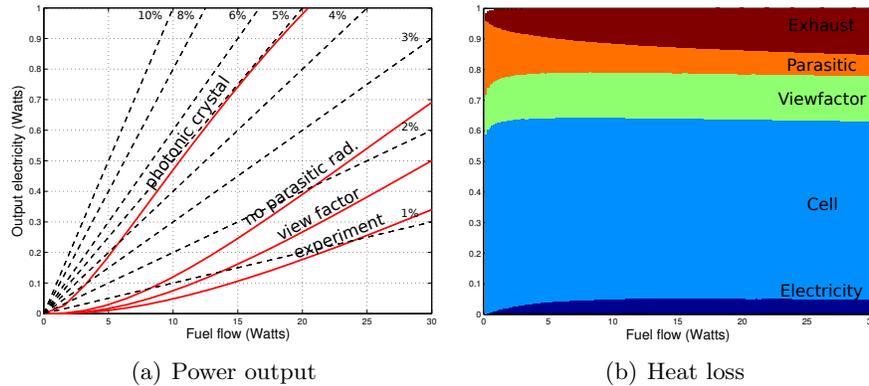Figure 4-2: Power generation and heat loss breakdown with the improvements to packaging and the addition of the Si/SiO_2 photonic crystal. In (a), the curves are (lowest to highest) the current system, improved view factor, eliminated side radiation, and added photonic crystal. The improvements are accumulative. The heat loss breakdown is for the system with all improvements made.

air is only 20% oxygen, there will be a five-fold increase in flow through the microreactor for a given fuel flow. Thus, the exhaust losses increase by roughly a factor of five unless there is recuperation. It would be difficult to obtain the high temperatures necessary for TPV without recuperation.

Pressure drop is another consideration. The air needs to be pushed through the system, either actively by a pump or fan or passively by convection or the Venturi effect. The natural methods are fairly weak and the active methods require electricity. We pay a premium for pumping because generating electricity and pumping are both inefficient. Doing 100 mW (about 120 sccm across 0.5 atm) of work on the air will likely require burning at least an additional 10 W of fuel. Either way, pressure drop must be kept to a minimum.

These requirements present a tough problem in systems optimization but it does not seem impossible. It is truly exciting to be at the point where we have enough experience and enough knowledge of the individual components to begin to tackle these problems. The work done in this thesis on modeling will prove invaluable in working towards a portable power generator design. The experimental work done to construct a system will be similarly beneficial as a platform on which to test new microreactor, photonic crystals, or cells.

Appendix A

TPV Cell Packaging

The cells for this work were hand selected from about 500 existing cells grown at Lincoln Labs. IV curves were measured for each growth run and the better runs were subject to more extensive characterization. Electrically, cells were selected for high shunt resistance and low series resistance. Mechanically, they were selected for being free of scratches and chips, and the metallization being well adhered and in good condition. Two sets of two matched cells from the same wafer and one set of four were selected and packaged by indium reflow soldering to a copper submount. Indium solder was necessary because the cells can be damaged by subjecting them to high temperatures. Packaging was performed by Leo Missaggia from Lincoln Laboratory. He prepared copper submounts by cleaning and sputtering gold then masked and evaporated indium where the cell would go. The indium was reflowed in a vacuum oven with the cell held in place by a jig. The copper submount serves as the negative contact. The positive contact was a metallized ceramic pad, and contact was made to the cell's bus bar by wire bonding. An antireflection coating
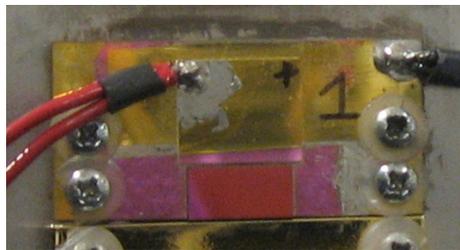
Figure A-1: Photograph of packaged GaInAsSb cell mounted on aluminum heat sink.

was deposited by Peter O'Brien at Lincoln Laboratory.

Appendix B

Microreactor Packaging

The microreactor used for this work were fabricated by Mohammad Araghchini at MIT. The process flow and masks are detailed in Appendix B of Ref. [23]. After receiving the die-sawed wafer, there were several steps that needed to be taken before using the microreactor: the catalyst had to be loaded and glass tubes had to be attached for the fuel/oxygen inlet and exhaust outlet. Finally, the microreactor with tubes had to be packaged in a housing to allow for easy handling and testing.

B.0.1 Catalyst Loading

A wash-loading technique similar to the one described in Section 4.2.2 of Ref. [23] was used to load the catalyst. The platinum catalyst was injected into the microreactor as a slurry and allowed to dry inside the channel. The slurry was prepared by from 5% Pt on γ-alumina, 325 mesh (Sigma Aldrich 311324). The catalyst was mixed in a 10:1 weight

Figure B-1: Cross section of microreactor showing the etched channel. Left has catalyst and right does not.

ratio with water and ground for one hour in a mortar and pestle. The slurry was further diluted with water to 20:1. The catalyst would remained in suspension for five minutes. The slurry was loaded into the reactors with a syringe. The reactors were heated to 80°C in a horizontal orientation for one hour to evaporate the water. The process was repeated except the catalyst was dried with the reactors turned over, coating both the top and bottom of the channel with catalyst. Note that the catalyst slurry has a limited lifetime of several weeks.

B.0.2   Glass Brazing

Two Pyrex glass capillary tubes serve as both the fuel/oxygen inlet and exhaust outlet as well as mechanical support. The capillaries were 0.550 mm OD and were purchased from Vitrocom. The tubes were glass brazed to the silicon microreactor. Glass brazing is similar to reflow soldering in microelectronics except the solder paste is replaced by solder glass: a mixture of powdered glass (glass frit) and a binder. The solder glass is mixed with a solvent and applied as a paste and allowed to dry then fired. During the firing process, the binder burns off and the glass reflows to form a hermetic seal. Sem-Com SCC-7 was used.

A stainless steel jig was used to hold the reactors and tubes in place when applying the braze and during firing. The firing process is hot enough to soften the glass tubes, making it necessary to support them to prevent excessive deformation. Having straight tubes is critical to accurately positioning the microreactor near the cells to achieve a high view factor. The brazing jig is shown in Fig. B-2.

When the reactors and tubes are in place, the glass braze is mixed with water. The consistency of the paste should be that of thin Plaster of Paris. If too much or too little water is added, the braze won't seal properly. The mixture is applied to the joints between the capillary and microreactor with a needle and formed into a fillet. The braze dries fast and it is necessary to complete each joint while the paste is still fluid (about 30 seconds). When finished, the braze is saved by adding water and mixing all the braze into a thin paste. The braze is then allowed to dry at room temperature and ground back into a fine powder.

The whole jig is placed in a box furnace and fired. The firing process involves heating
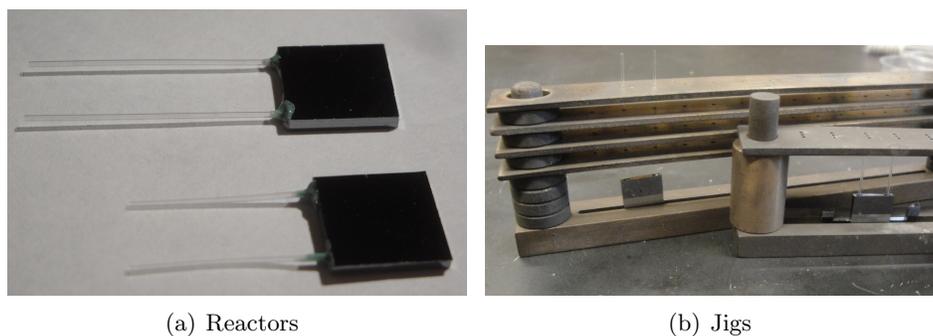
(a) Reactors   (b) Jigs

Figure B-2: New (rear) and old (front) brazing jigs and reactors brazed in each jig. The new jig produces longer and straighter tubes by supporting the tubes at multiple points.

to 350°C for two hours to burn off the binder. The temperature is then ramped at a rate of 10°C per minute to 690°C where it is maintained for two hours to reflow the braze. The furnace is then cooled at 1°C per minute to 400°C, when it can be shut off. The reactors can be removed when they reach room temperature.

B.0.3 Microreactor Mounting

The other ends of the capillary tubes are epoxied into an aluminum reactor frame. The epoxy must provide a vacuum tight seal between both the inlet and outlet and the vacuum chamber. After testing numerous adhesives described in Table B.1, Loctite Hysol 1C was found to work best although its performance is not satisfactory. After extended operation (30 minutes) the epoxy on the outlet tube burns, allowing air to enter the vacuum chamber. The epoxy was mixed according to the manufacture's directions and was applied using a toothpick while the microreactor and frame were held in a jig. The cure schedule used was 3 hours at 65°C.

Epoxy	Vendor	Description	Results
5 minute	Devcon	General purpose 2 part epoxy	Easy to apply, decent life, surprisingly one of the best
Aremcobond 526N	Aremco	General purpose high temperature 2 part epoxy	A little better than 5 minute epoxy but difficult to apply
Hysol 1C	Loctite	General purpose 2 part epoxy rated for vacuum	A little better than 5 minute epoxy
Celva 2	Dunniway	Vacuum sealing and repair repair, 1 part	Poor gap filling
Fiberbond 380	Aremco	Sealing glass fibers to feruls, 1 part	Poor gap filling
Ceramabond 503	Aremco	Halogen bulbs, encapuslating heating elements, 1 part	Poor adhesion
Silver epoxy	Aremco	High temperature thermal epoxy, 1 part	Tended to crack
Corrpaint	Aremco	Coating boilers, industrial pipelines, etc., 1 part	Poor gap filling

Table B.1: Epoxies tested for mounting the microreactor to the reactor frame.

Appendix C

Filter Fabrication Process

Starting materials: bonded pair of microreactor wafers (finished but not diced). The microractor process can be found in Appendix B of Ref. [23].

Step	Fab	Machine	Wafer	Action
1	ICL	RCA	1,2 (bonded)	RCA
2	ICL	DCVD	1,2 (bonded)	Deposit 5331A SiO2
3	ICL	DCVD	1,2 (bonded)	Deposit 2285A poly
4	ICL	Tube 5B	1,2 (bonded)	Anneal
5	ICL	RCA	1,2 (bonded)	RCA
6	ICL	DCVD	1,2 (bonded)	Deposit 5499A SiO2
7	ICL	DCVD	1,2 (bonded)	Deposit 2357A poly
8	ICL	Tube 5B	1,2 (bonded)	Anneal
9	ICL	RCA	1,2 (bonded)	RCA
10	ICL	DCVD	1,2 (bonded)	Deposit 5673A SiO2
11	ICL	DCVD	1,2 (bonded)	Deposit 2431A poly
12	ICL	Tube 5B	1,2 (bonded)	Anneal
13	ICL	RCA	1,2 (bonded)	RCA
14	ICL	DCVD	1,2 (bonded)	Deposit 2836A SiO2
15	ICL	Tube 5B	1,2 (bonded)	Anneal

Bibliography

[1] A. Manthiram. Materials aspects: an overview. In G. Nazri and G. Pistoia, editors, *Science and Technology of Lithium Batteries*, chapter 1, pages 3–37. Springer, 2003.

[2] J. Goldstein, I. Brown, and B. Koretz. New developments in the electric fuel ltd. zinc/air system. *Journal of Power Sources*, 80(1-2):171 – 179, 1999.

[3] B. Kumar, J. Kumar, R. Leese, J. P. Fellner, S. J. Rodrigues, and K. M. Abraham. A solid-state, rechargeable, long cycle life lithium–air battery. *Journal of The Electrochemical Society*, 157(1):A50–A54, 2010.

[4] A. Kamitani, S. Morishita, H. Kotaki, and S. Arscott. Miniaturized microDMFC using silicon microsystems techniques: performances at low fuel flow rates. *J. Micromech. Microeng.*, 18:125019, 2008.

[5] V. Bagotsky. *Fuel Cells: Problems and Solutions*. Wiley, 2009.

[6] A.. Gomez, J. J. Berry, S. Roychoudhury, B. Coriton, and J. Huth. From jet fuel to electric power using a mesoscale, efficient stirling cycle. *Proceedings of the Combustion Institute*, 31(2):3251 – 3259, 2007.

[7] A. McNaughton. Commercially available generators. In D.M. Rove, editor, *CRC Handbook of Thermoelectrics*, chapter 36, pages 459–469. CRC Press, 1995.

[8] S. McIntosh and R. J. Gorte. Direct hydrocarbon solid oxide fuel cells. *Chem Rev.*, 104:4845–4865, 2004.

[9] A. H. Epstein. Millimeter-scale, micro-electro-mechanical systems gas turbine engines. *Journal of Engineering for Gas Turbines and Power*, 126(2):205–226, 2004.

[10] D. M. Rowe. Miniature semiconductor thermoelectric thermoelectric devices. In D.M. Rove, editor, *CRC Handbook of Thermoelectrics*, chapter 35, pages 411–457. CRC Press, 1995.

[11] S. B. Schaevitz. *A MEMS Thermoelectric Generator.* PhD thesis, Massachusetts Institute of Technology, 2000.

[12] H.H. Kolm. Solar-battery power source. Quarterly progress report, solid state research, group 35, MIT-Lincoln laboratory, 1956.

[13] M. W. Dashiell, J. F. Beausang, H. Ehsani, G. J. Nichols, D. M. Depoy, L. R. Danielson, P. Talamo, K. D. Rahner, E. J. Brown, S. R. Burger, P. M. Fourspring, W. F. Topper Jr., P. F. Baldasaro, C. A. Wang, R. K. Huang, M. K. Connors, G. W. Turner, Z. A. Shellenbarger, G. Taylor, J. Li, R. Martinelli, D. Donetski, S. Anikeev, G. L. Belenky, and S. Luryi. Quaternary InGaAsSb thermophotovoltaic diodes. *Electron Devices, IEEE Transactions on*, 53(12):2879–2891, Dec. 2006.

[14] T. Schlegl, F. Dimroth, A. Ohm, and A. W. Bett. TPV modules based on GaSb structures. In *Sixth Conference on Thermophotovoltaic Generation of Electricity*, pages 285–293. AIP, 2004.

[15] I. Celanovic, N. Jovanovic, and J. Kassakian. Two-dimensional tungsten photonic crystals as selective thermal emitters. *Applied Physics Letters*, 92(19):193101, 2008.

[16] P. F. Baldasaro, E. J. Brown, D. M. Depoy, B. C. Campbell, and J. R. Parrington. Experimental assessment of low temperature voltaic energy conversion. In *The first NREL conference on thermophotovoltaic generation of electricity*, pages 29–43. AIP, 1995.

[17] B. Wernsman, R. R. Siergiej, S. D. Link, R. G. Mahorter, M. N. Palmisiano, R. J. Wehrer, R. W. Schultz, G. P. Schmuck, R. L. Messham, S. Murray, C. S. Murray, F. Newman, D. Taylor, D. M. Depoy, and T. Rahmlow. Greater Than 20% Radiant Heat Conversion Efficiency of a Thermophotovoltaic Radiator/Module System Using Reflective Spectral Control. *IEEE Transactions on Electron Devices*, 51:512–515, March 2004.

[18] L. M. Fraas, J. E. Avery, and H. X. Huang. Thermophotovoltaic furnacegenerator for the home using low bandgap gasb cells. *Semiconductor Science and Technology*, 18(5):S247, 2003.

[19] E. Doyle, K. Shukla, and C. Metcalfe. Development and demonstration of a 25 watt thermophotovoltaic power source for a hybrid power system. Technical Report TR04-2001, National Aeronautics and Space Administration, August 2001.

[20] Y. Wenming, C. Siawkiang, S. Chang, X. Hong, and L. Zhiwang. Research on micro-thermophotovoltaic power generators with different emitting materials. *Journal of Micromechanics and Microengineering*, 15(9):S239, 2005.

[21] O. Nielsen. *A thermally efficient micro-reactor for thermophotovoltaic power generation*. PhD thesis, Massachusetts Institute of Technology, 2006.

[22] A. Carlos Fernandez-Pello. Micropower generation using combustion: Issues and approaches. *Proceedings of the Combustion Institute*, 29(1):883 – 899, 2002.

[23] B. S. Blackwell. *Design, fabrication, and characterization of a micro fuel processor*. PhD thesis, Massachusetts Institute of Technology, 2008.

[24] L. Arana. *High-temperature microfluidic system for thermally-efficient fuel processing*. PhD thesis, Massachusetts Institute of Technology, 2003.

[25] B. Bitnar. Silicon, germanium and silicon/germanium photocells for thermophoto-voltaics applications. *Semiconductor Science and Technology*, 18(5):S221, 2003.

[26] A. W. Bett and O. V. Sulima. Gasb photovoltaic cells for applications in tpv generators. *Semiconductor Science and Technology*, 18(5):S184, 2003.

[27] C. A. Wang, H. K. Choi, S. L. Ransom, G. W. Charache, L. R. Danielson, and D. M. DePoy. High-quantum-efficiency 0.5eV GaInAsSb/GaSb thermophotovoltaic devices. *Applied Physics Letters*, 75(9):1305–1307, 1999.

[28] A. Licciulli, D. Diso, G. Torsello, S. Tundo, A. Maffezzoli, M. Lomascolo, and M. Mazzer. The challenge of high-performance selective emitters for thermophoto-voltaic applications. *Semiconductor Science and Technology*, 18(5):S174, 2003.

[29] S. Y. Lin, J. Moreno, and J. G. Fleming. Three-dimensional photonic-crystal emitter for thermal photovoltaic power generation. *Applied Physics Letters*, 83(2):380 –382, jul 2003.

[30] D. L. Chubb. *Fundamentals of Thermophotovoltaics*. Elsevier, 2007.

[31] M. F. Modest. *Radiative Heat Transfer*. McGraw-Hill, 1993.

[32] Y. P. Varshni. Temperature dependence of the energy gap in semiconductors. *Physica*, 34(1):149 – 154, 1967.

[33] D. Aiken, M. Stan, C. Murray, P. Sharps, J. Hills, and B. Clevenger. Temperature dependent spectral response measurements for III-V multi-junction solar cells. In *Photovoltaic Specialists Conference, 2002. Conference Record of the Twenty-Ninth IEEE*, pages 828–831, May 2002.

[34] D. Martin and C. Algora. Temperature-dependent GaSb material parameters for reliable thermophotovoltaic cell modeling. *Semiconductor Science and Technology*, 19:1040–1052, July 2004.

[35] J. Charles, I. Mekkaoui-Alaoui, and G. Bordure. A critical study of the effectivelness of the singe and double exponential models for I-V characterization of solar cells. *Solid State Electronics*, 28(8):807–820, 1985.

[36] M. Chegaar, Z. Ouennoughi, and A. Hoffmann. A new method for evaluating illuminated solar cell parameters. *Solid State Electronics*, 45:293–296, 2001.

[37] S. Hegedus. Current-voltage alaysis of a-Si and a-SiGe solar cells including voltage-dependant photocurrent collection. *Progress in photovoltaics*, 5:151–168, 1997.

[38] MATLAB. *fminsearch*. The MathWorks, Natick, MA, 2008.

[39] P. Ashburn. A theoretical and experimental study of recombination in silicon p-n junctions. *Solid State Electronics*, 18:569–577, June 1975.

[40] J. M. Gee, J. B. Moreno, S. Lin, and J. G. Fleming. Selective emitters using photonic crystals for thermophotovoltaic energy conversion. In *Photovoltaic Specialists*

Conference, 2002. Conference Record of the Twenty-Ninth IEEE, pages 896–899, May 2002.

[41] R. C. N. Pilawa-Podgurski, N. A. Pallo, W. R. Chan, D. J. Perreault, and I. L. Celanovic. Low-power maximum power point tracker with digital control for thermophotovoltaic generators. In *Applied Power Electronics Conference and Exposition (APEC), 2010 Twenty-Fifth Annual IEEE*, pages 961 –967, feb. 2010.

[42] A. Roth. *Vacuum Sealing Techniques*. Pergamon Press, 1966.

[43] M. Pirani and J. Yarwood. *Principles of Vacuum Engineering*. Chapman and Hall, 1961.